Manuscript accepted for publication in Journal of Structural Geology.

It has not yet been assigned a DOI or undergone the proofreading process. Subsequent version of the manuscript may have slightly different content.

@driptadutta

Deformation mechanisms and characteristics of the meta-BIFs from an early Proterozoic shear system of the Southern Granulite Terrane (SGT), India

Dripta Dutta[1#], Santanu Misra[1*], and Shreya Karmakar[2]

[1] Experimental Rock Deformation Laboratory, Department of Earth Sciences, Indian Institute of Technology Kanpur, Uttar Pradesh 208 016, INDIA
[2] Department of Geological Sciences, Jadavpur University, West Bengal 700 054, INDIA

email (ORCiD ID)
dripta.dutta@gmail.com, driptad@iitk.ac.in (0000-0001-9247-6388)
* corresponding author; smisra@iitk.ac.in (0000-0002-2364-1965)

Abstract

We studied three samples of Banded Iron Formation (BIF) rocks from Southern Granulite Terrane (SGT) of India, which was metamorphosed at high-pressure granulite facies and exhumed from 40-50 km depth. We examined the microstructure, texture, and deformation mechanisms of the primary minerals (quartz, magnetite, and hematite). Microstructures, variations in size and shape of quartz grains suggest that the three samples deformed to different intensities and temperatures. The EBSD derived CPOs for quartz and magnetite grains are strong, implying dislocation creep as the dominant mechanism. The presence of distinct subgrains in magnetite, rare in natural samples, attests to the same. Furthermore, twinning on {111}, as evident from the misorientation angle and axis distributions, indicates ductile deformation of magnetite below 400 °C. Subgrain boundary trace analysis in selected magnetite grains reveals that multiple-slip planes {111}, {110}, and {100} were operational. Topotaxial replacement, via redox reaction, of magnetite grains along their octahedral planes by hematite is evident. Well-developed CPOs but low (<1°) GOS values of both magnetite and hematite grains suggest that recovery processes in these were rapid. Post-replacement deformation was weak and did not affect the hematite CPOs that were inherited from the relatively more deformed host magnetite grains.

Keywords: EBSD; Quartz CPO; Magnetite CPO, Hematite CPO; Subgrain boundary trace analysis; Magnetite-Hematite topotaxy

1. Introduction

Banded Iron Formations (BIFs) are deep-sea sedimentary deposits of alternating Fe- and silica-rich layers. They are primarily reported from the Precambrian cratons across the globe and particularly abundant in the Eoarchean-Paleoproterozoic time (Klein, 2005; Mukhopadhyay, 2020). The BIFs are a significant source of iron ores, and hence much of the previous research works focused on their origin (e.g., Konhauser et al., 2002; Kappler et al., 2005; Robbins et al., 2019), and more recently, their post-depositional metamorphism and deformation (Mendes and Lagoeiro, 2012; Ferreira et al., 2016; Egglseder et al., 2017; Zheng et al., 2018).

Studies aimed at understanding the ductile deformation mechanisms of the major constituent minerals in BIFs, such as quartz, hematite, and magnetite, have been of particular interest. To this end, previous workers have extensively examined naturally deformed samples (e.g., Morales et al., 2008a, 2008b; Barbosa and Lagoeiro, 2010; Rosière et al., 2013; Ávila et al., 2015) as well as experimentally deformed natural (Hennig-Michaeli, 1977; Siemes et al., 2008) and synthetic (Till et al., 2019 and references therein) specimens. Compressional tests performed on hematite crystals by Siemes et al. (2008) at 10^{-5} s^{-1} strain rate, demonstrated that r-twinning is favored over c-twinning at > 200 °C, whereas at room temperatures (~25 °C), the latter is dominant. Although Siemes et al. (2008) suggested that the basal glide (c)⟨a⟩ is activated at temperatures > 600 °C, Rosière et al. (2001) showed that under geological strain rates, (c)⟨a⟩ could well be active within the range 300–600 °C. For magnetite, the slip direction is always ⟨110⟩ (Hornstra, 1960). Experimental observations by Hennig-Michaeli and Siemes (1975) at 10^{-5} s^{-1} revealed {111}⟨110⟩ to be the dominant slip system in magnetite below 400 °C. Two other slip systems, {100}⟨110⟩ and {110}⟨110⟩, have also been reported to occur in magnetite grains deformed in the laboratory at ≥ 1100 °C and strain rates of 10^{-4}–10^{-5} s^{-1} (Till and Moskowitz, 2014). Although dislocation creep activity has been reported for these phases, microtextural evidence of intracrystalline deformation such as subgrains have rarely been encountered in naturally deformed hematite (Ferreira et al., 2016) and magnetite (Boyle et al., 1998; Mamtani et al., 2020) grains.

Another interesting subset of research concerning the Fe-oxides has been the topotaxial replacement of magnetite by hematite grains (Lagoeiro, 1998; Braga de Oliveira et al., 2020; Yin et al., 2022). Such a replacement is most commonly characterized by the parallelism of the basal (0001) planes of hematite to the octahedral (111) planes of magnetite, apart from few other topotactic relationships (Braga de Oliveira et al., 2020 and references therein). Lagoeiro (1998) also proposed that the newly precipitated hematite grains, unlike their host, are free of dislocations and thus weaker. The strength contrast between Fe-oxides and silicate phases such as quartz and feldspars, with or without involving water, have been widely addressed (Cannat, 1991; Siemes et al., 2003; Chernak et al., 2009; Till and Moskowitz, 2013; Gonçalves et al., 2015; Zheng et al., 2018). Gonçalves et al. (2015) conducted high-pressure-temperature experiments with natural and synthetic aggregates of BIFs and demonstrated that a feedback process operates during the deformation of quartz and Fe-oxide grains through stress transfer and dynamic recrystallization. They also showed that the quartz-rich layers act as the "*load-bearing framework*" during the deformation of the BIFs. The experiments, however, did not demonstrate any significant strength difference between hematite and magnetite.

In this contribution, we studied naturally deformed BIF samples from the Precambrian Southern Granulite Terrane of India and aim to present the deformation processes that have affected the BIFs. Our interest lies in elucidating the deformation behavior of the major constituent mineral phases (quartz, magnetite, and hematite) and the corresponding microstructural signatures, particularly the intergrowth textures of magnetite and hematite. We employed the SEM-based EBSD technique alongside petrographic studies to investigate the creep mechanisms that controlled the deformation of the silica-rich domains and evaluate the possibility of a topotaxial transformation of magnetite into hematite.

2. Geological background

The overall EW trending Cauvery Shear System (CSS), also referred to as Palghat-Cauvery Shear Zone System (Collins et al., 2007) or Cauvery Shear Zone (Chetty and Rao, 2006), with an areal extent of ~24,500 sq. km. (Geological Survey of India, 1995; Subramanian and Selvan, 2001), records ~2.4 Ga of the crustal evolutionary history of the Precambrian Southern

Granulite Terrane (SGT), which lies to the south of the Archean Dharwar craton in southern India (Ramakrishnan and Vaidyanadhan, 2008; Valdiya, 2016). The northern part of the SGT, known as the northern Granulite Block, comprises high-grade (> 800 °C) late Archean felsic orthogneisses. In contrast, Neoarchean metasediments and Mesoproterozoic felsic magmatic suites dominate the southernmost portion – the Madurai Block (Ghosh et al., 2004).

The CSS (**Fig. 1a,b**), a cluster of multiple shear zones (Chetty and Rao, 2006; Plavsa et al., 2015; Yellappa et al., 2016), separates these two blocks and mainly consists of granulite facies Neoarchean felsic orthogneisses that host mafic-ultramafic granulites interlayered with the metamorphosed supracrustal Algoma-type Banded Iron Formations (BIF) (Brandt et al., 2014). This package was metamorphosed at ~750–850 °C temperatures and ~12–14 kbar pressures, followed by decompression and cooling up to 600 °C and ~6 kbar (Karmakar et al., 2017; Chowdhury and Chakraborty, 2019). Meißner et al. (2002) reported younger (~500 Ma) Sm-Nd garnet whole rock ages of gneisses from ~150 km southwest of Namakkal (**Fig. 1b**) and correlated it to an episode of enhanced fluid activity within the shear zone. However, they did not comment on the nature of the fluid(s). Moreover, Chowdhury and Chakraborty (2019) studied the mafic-ultramafic granulites from the shear zone and attributed the presence of amphibole rims on the clinopyroxene grains to a hydrous retrograde event. Using pseudosection modelling Chowdhury and Chakraborty (2019) further suggested that the fluid (H_2O-bearing) ingress occurred at $\leq$700 °C.

The elongated BIF bands in the study area are 5–20 m thick and are intensely folded regionally into a series of antiforms and synforms with steep E-W trending axial planes. The BIF layers are widest at the hinges and thinner at the limbs. The present structural architecture of the BIFs results from two phases of deformations, D_1 and D_2, both of which occurred at granulite facies conditions. The gneissosity of the host orthogneiss developed during D_1, whereas the N-S compression induced folding characterizes D_2 (Talukdar et al., 2020). The latter also produced the E-W trending linear fabric, particularly at the hinges, with a gentle easterly plunge, defined by the elongated streaks of magnetite and quartz alterations (Talukdar, 2015).

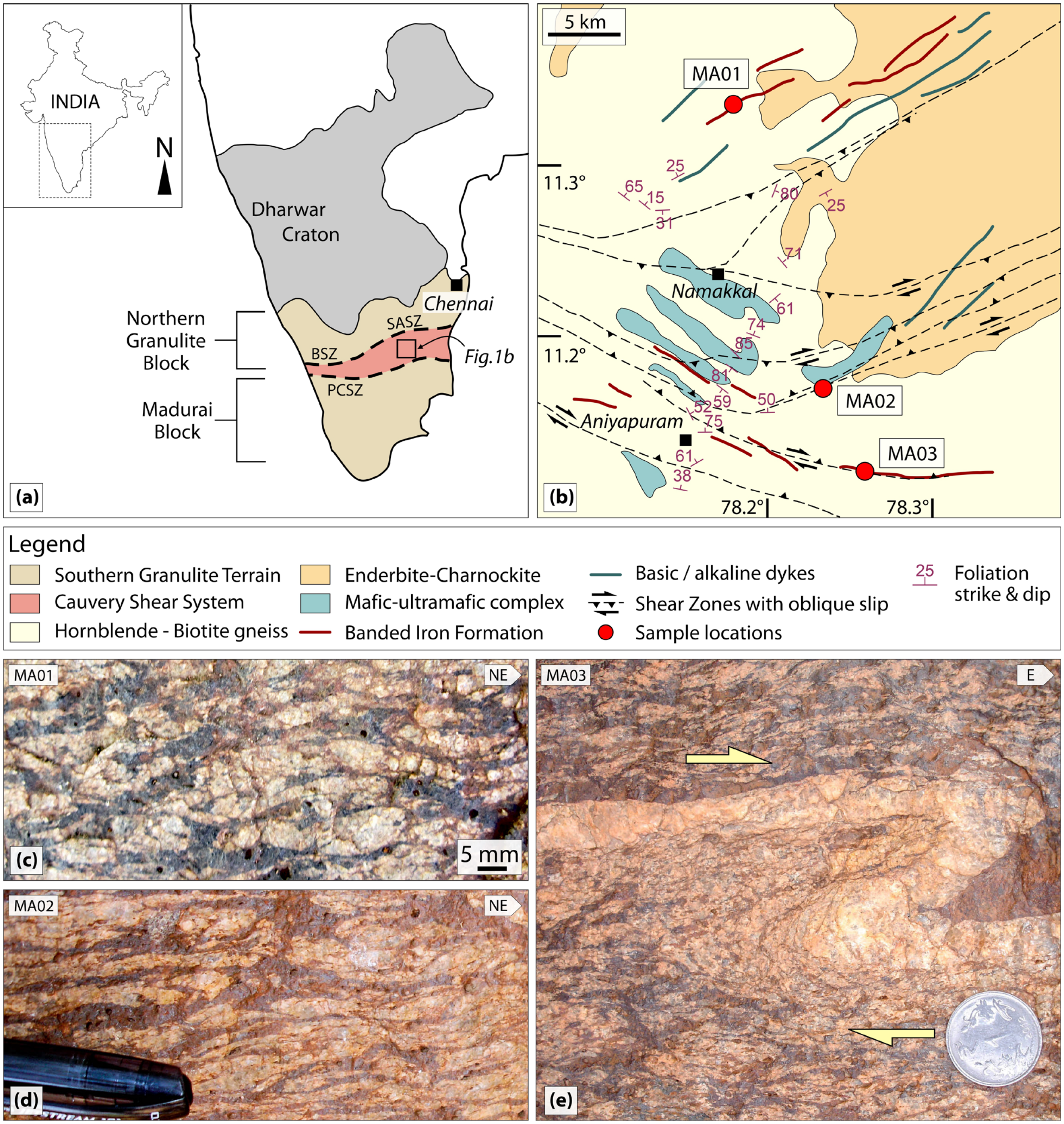

Fig.1. *Regional and geological maps of the study area, and field photographs.* ***(a)*** *Location of the Dharwar Craton, Southern Granulite Terrane and Cauvery Shear System (CSS) in southern India.* ***(b)*** *Study area in the vicinity of town Namakkal along with the sample locations.* ***(a)*** *is reproduced from Sharma (2010).* ***(b)*** *is redrawn after Dutta et al. (2011) and Brandt et al. (2014). The shear zones and the structural data are from Plavsa et al. (2015). BSZ: Bhavani Shear Zone, SASZ: Salem Attur Shear Zone, PCSZ: Palghat Cauvery Shear Zone.* ***(c-e)*** *Interlayered dark and light bands, rich in Fe-oxides and quartz, respectively, in the BIF. The layers define the foliation. Isolated folded quartz vein in* ***(e)*** *indicates foliation parallel dextral ductile shearing.*

Three meta-BIF samples from the SGT were collected and examined. The locations of the samples are in the vicinity of the town Namakkal, Tamil Nadu and well within the CSS (**Fig. 1b**). Overall, the three samples exhibit a distinct banded proto-mylonitic appearance of dark-coloured Fe-oxide and light-coloured quartz rich layers (**Fig. 1c-e**). In addition to these primary minerals, the samples also contain pyroxenes and plagioclase as accessories and occur as porphyro-blasts and -clasts, respectively. The layers define the foliation (XY plane of the strain ellipsoid) in the rock. Lineation (X-axis of the strain ellipsoid) is defined by the stretching of both Fe-oxide and quartz aggregates. In the macroscopic scale the bands are long, lenticular in shape, mostly symmetrical and discontinuous.

3. Methodologies

3.1 Optical microscopy

Polished thin sections, cut along the stretching lineation and perpendicular to the foliation (XZ-section), were prepared from the three samples of the meta-BIFs. These were studied using an optical microscope, under both plane and cross-polarized transmitted light. Through this technique, we intended to identify the major minerals and overall deformation-related microstructures.

3.2 Electron backscatter diffraction

Three rock chips of approximately 5.0×5.0 mm^2 were cut along XZ planes. The chips were about 2.5 mm thick. One of the surfaces of each chip was finally polished with colloidal silica solution. Electron backscattered diffraction (EBSD) data was then acquired from the polished surface using JEOL JSM-7100F FE-SEM – at an accelerating voltage of 20 kV, a beam current of 13 nA, 20 mm working distance, 70° sample tilt, and at low vacuum mode. The data were indexed automatically using the inorganic crystal structure database (ICSD) of the AZtec software (Oxford Instrument). The indexing rate was > 90% for all the scans, whereas the frequency varied between 12–21 Hz. The step size ranged from 0.05 to 3.0 µm. Finer step size was chosen for smaller scan areas to collect detailed intragranular orientation information. Thin, adhesive copper tapes were used to prevent charging of the sample surface during data acquisition. The EBSD derived data were postprocessed in MATLAB 2020b using MTEX toolbox v5.6.0 (Hielscher and Schaeben, 2008; Bachmann et al., 2010). Poorly indexed data points (mean angular deviation > 1.0°) were removed. The phase and orientation (IPF-X) maps were obtained after reconstructing the grains using the Voronoi decomposition algorithm (Bachmann et al., 2011) and a threshold misorientation angle of 10°. Furthermore, grains with less than three indexed pixels were discarded.

3.2.1 Crystallographic preferred orientations

The pole figures of quartz, magnetite and hematite crystals were plotted on equal area, lower hemisphere stereonets using one point per grain (to avoid the bias from coarse grains) and de la Vallée Pousin kernel halfwidth of 10°. Mainprice et al. (2015) argued that the one point per grain model is less appropriate for quantitative texture analysis than the volume fraction approach. Hence, although we report texture (J_{ODF}; Bunge, 1982) and misorientation (M) indices (Skemer et al., 2005) calculated using all the indexed points and one point per grain, we base our interpretations on the results of the former method. The number of symmetrically equivalent directions vary amongst different crystallographic axes/poles, hence, comparing their CPO strengths based on the pole figure intensity (pfJ) values could be erroneous. Consequently, to facilitate error free comparison, we report the product (mpfJ) of a CPO pfJ value and the corresponding multiplicity factor (m) (Mainprice et al., 2015).

3.2.2 Misorientation analysis

Misorientation angle distributions (MADs) were plotted for pairs of both adjacent/neighbor and random grains of quartz, magnetite, and hematite, to assess the extent of deformation and identify the presence of twinning (Wheeler et al., 2001; Ferreira et al., 2016; Barbosa et al., 2020). The angle (α) between the trace of a low-angle (quartz: 2–<10°; magnetite & hematite: 1–<10°) boundary and the projection of its corresponding low-angle misorientation axis (LAX) on the plane of observation (XZ-plane) was calculated. If $\alpha < 15°$, the related subgrain boundary is certainly composed of edge dislocations only – a tilt boundary (**Fig. 2a**). However, if $\alpha > 75°$, the subgrain boundary could either be a tilt or twist (**Fig. 2b-d**). Subgrain boundaries with traces oblique to their LAXs i.e., $15° \leq \alpha \leq 75°$ are categorized as general and possess both tilt and twist characteristics (Hull and Bacon, 2011). The LAXs for each

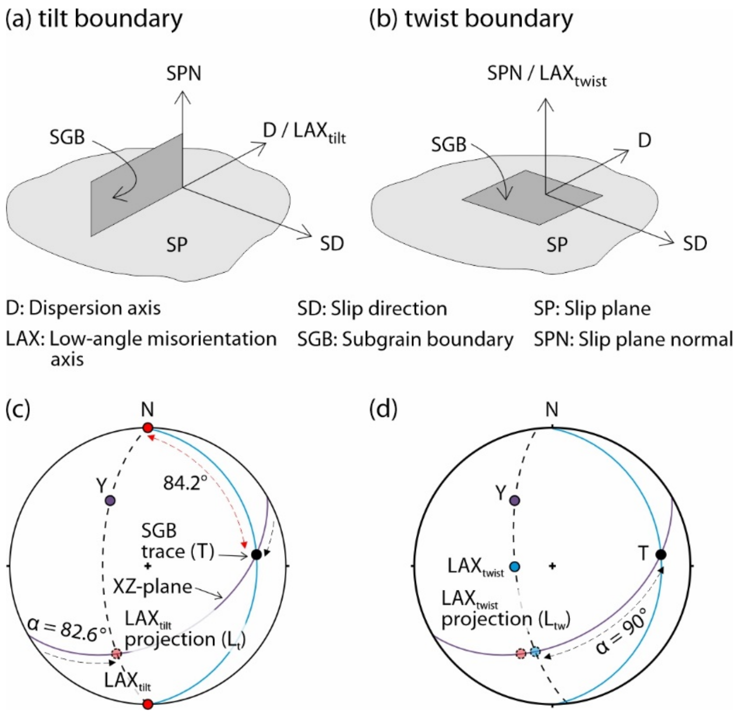

Fig. 2. *Definition diagram showing subgrain boundaries (SGBs) and their angular relationship to the low-angle misorientation axes (LAXs). The orientations are arbitrarily chosen and plotted on a geographic reference frame to ease comprehension. They are represented as dip amount→dip direction and plunge amount→plunge direction for planes and lines, respectively. The stereoplots are lower hemisphere equal area projections.* ***(a)*** *Tilt subgrain boundary.* ***(b)*** *Twist subgrain boundary. Both* ***(a)*** *and* ***(b)*** *are reproduced from Lloyd (2004). The projection (L_t; 37°→ 191°) of the low-angle misorientation axis (LAX_{tilt}; 0°→ 180°) and the trace (T; 22°→ 84°) of the corresponding tilt subgrain boundary (22°→ 90°), on the XZ-plane (45°→150°) in* ***(c)*** *make an angle $\alpha > 75°$. Y (45°→330°) represents the pole to the XZ-plane.* ***(d)*** *The angle α between L_{tw} (33°→199°) and T will also be >75° if the SGB is twist because the LAX_{twist} (68°→ 270°) is normal to the SGB.*

of the three categories were then plotted on separate inverse pole figures (IPFs) to determine the dominant slip-system in quartz grains. IPFs with ≥10 data points were contoured to multiples of uniform density (m.u.d). Otherwise, they are presented as scatter plots. The angular ranges of the neighbor pair MAD peaks were visually identified. The misorientation axes corresponding to those high angles (HAXs) were calculated for both magnetite and hematite grains and the orientations were plotted on crystal reference frames, as IPFs, to identify the twin axes. Furthermore, grain orientation spread (GOS) maps were obtained from specific regions of samples MA02 and MA03, where both magnetite and hematite grains are dominant. They are presented to recognize any relative differences in the accumulated strain between magnetite and hematite.

3.2.3 Subgrain boundary trace analysis

The extent of intragranular plastic deformation is better visualized in maps that depict the deviation of each orientation within a grain to its mean orientation (mis2mean). To identify the potential magnetite slip system(s), we visually inspected the mis2mean maps and targeted eight grains which exhibit prominent variations in the intragranular orientations. We further noted that LAXs calculated from similarly oriented subgrain boundary traces were less dispersed, exhibited point distributions, than those derived from a set of traces that are at high angle to each other. Hence, one or more set(s) of nearly parallel subgrain boundary traces within a grain were chosen by manually drawing a polygon (using MTEX's *selectPolygon* feature) that enclosed all of them. The nature of all the boundaries, from within a set, was identified (outlined in Sec. 3.2.2) and only the tilt and twist ones were further analyzed, separately (e.g., Prior et al., 2002; Reddy et al., 2007). We have avoided the '*general*' boundaries from this analysis because their deconvolution into tilt and twist elements could not be performed. See supplementary text (S1) for the script developed for and used in this study to perform the *subgrain boundary trace analysis*.

Deriving misorientation axes for lower misorientation angles could be erroneous, but the associated error decreases as the misorientation angle is increased (Prior, 1999; Reddy and Buchan, 2005). Thus, subgrain boundaries associated with ≥7° misorientations were preferably selected. In some cases, a lower angular limit of 4 or 5° were chosen so that at least 10 subgrain boundary traces could be analyzed. For the tilt boundaries, the mean direction of a set of subgrain boundary traces and the misorientation axis maximum were used to estimate the average subgrain boundary wall orientation. The slip plane normal (SPN), parallel to the subgrain boundary wall and perpendicular to the misorientation axis maximum, was calculated next, followed by the slip direction (pole to the subgrain boundary wall) (**Fig. 2a**). In the case of twist boundaries, the misorientation axis maximum is parallel to the slip plane normal, which is perpendicular to both the subgrain boundary wall and the slip direction (SD) (**Fig. 2b**) (Hull and Bacon, 2011). We also derived the dispersion axis from the orientation data enclosed by the polygon using the principal geodesic analysis (PGA - *https://github.com/zmichels/CVA*) code of Michels et al. (2015).

Once all the parameters were plotted on the specimen reference frame, a lower hemisphere equal area net, the orientations of ⟨001⟩, ⟨110⟩, and ⟨111⟩ corresponding to the grain mean orientation were used to obtain the possible slip systems for the magnetite grains (Reddy et al., 2007). However, the plots of SPN or SD, predicted using our script, did not always coincide perfectly with those of ⟨001⟩, ⟨110⟩, and ⟨111⟩, and hence the closest neighbor was considered as the possible SPN or SD.

4. Results

4.1 Petrography, grain size and deformation microstructures

The petrographic observations in all samples reveal the presence of quartz, clino- and orthopyroxenes, and feldspar (in decreasing abundance) apart from the opaques (Fe-oxides), which are present as thin bands, thickening occasionally, and define the trace of the foliation on the planes of observation (**Fig. 3a-d**).

Quartz grains show a variety of microstructures and hence are of particular interest in the samples. In MA01, most of the quartz grains are euhedral, moderate to coarse-grained, and blocky (**Fig. 3a**). However, these grains, collectively, define ribbons (~1 mm thick) that are wavy but sub-parallel to the foliation (**Fig. 3a**). The sample MA02 has quartz ribbons that are stretched parallel to the foliation (**Fig. 3b**). In MA03, the quartz grain-sizes vary across the trace of the foliations. The foliation-parallel ribbons, made up of coarse, elongated relict grains, are sandwiched between layers of dynamically recrystallized finer quartz grains (**Fig. 3c,d**). In contrast to both MA01 and MA02, MA03 has more pyroxene porphyroblasts and plagioclase porphyroclasts (**Fig. 3**). The pyroxene grains are relatively more euhedral than the quartz grains with the thin quartz ribbons warped around (**Fig. 3c**). Some of the plagioclase grains, with bent twin planes, host prismatic orthopyroxenes (**Fig. 3c,** inset). The larger grains of orthopyroxene and plagioclase are sheared (**Fig. 3c**) and often suggest opposite senses of ductile shear (Dutta and Mukherjee, 2019).

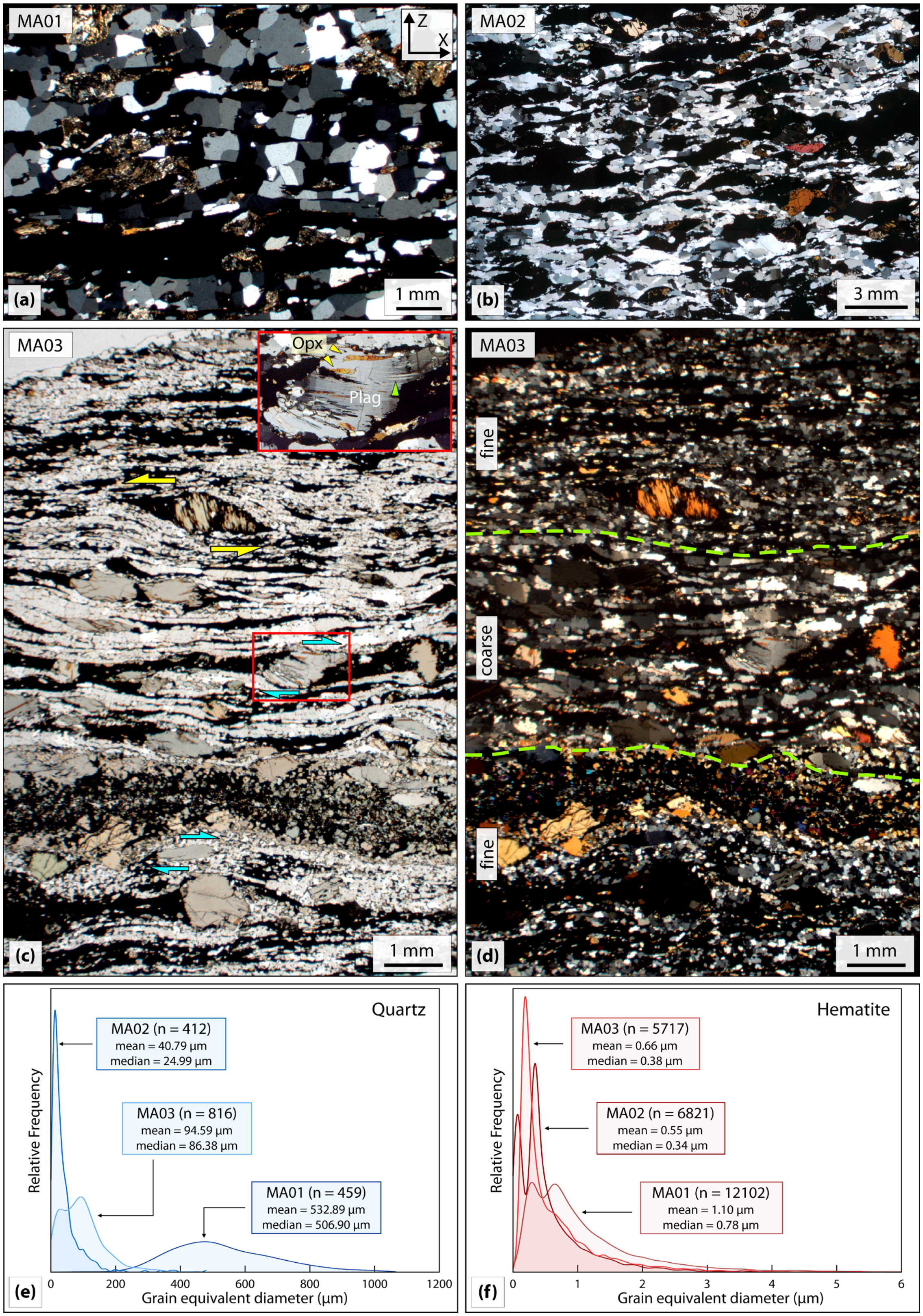

Fig. 3. *Thin-section photomicrographs and grain-size distribution plots.* ***(a)*** *Ribbons of equant and blocky quartz grains oriented parallel to the foliation.* ***(b)*** *Stretched quartz ribbons with*

*lobate quartz grain boundaries. The Fe-oxide rich layers (dark colored), as seen under optical microscope in **(c)** plane- and **(d)** cross-polarized lights, define the dominant foliation. Selected ductile kinematic indicators exhibiting opposite senses are present. The shear senses are marked with half-arrows. The cross-polarized version of the plagioclase porphyroclast (demarcated with red a rectangle) is shown as an inset for clearer perceptibility of the bent orthopyroxene laths (yellow arrowheads) and twin planes (green arrowhead). A layer of relatively coarser quartz grains in **(d)** is sandwiched between domains of fine-grained quartz. The grain-size (equivalent diameter) frequency curves for **(e)** quartz and **(f)** hematite corresponding to the three samples. The bimodal distribution of the quartz grains as noted for sample MA02 in **(d)** is also prominent in **(e)**. n = number of grains used for the grain size analysis. The kinematic axes for all the photomicrographs are oriented as illustrated in **(a)**.*

Using the EBSD data, we measured the sizes (equivalent diameter) of quartz and hematite grains. Magnetite grains are excluded from this analysis because reactions make it unreliable. We noted that both mean and median of the quartz grain size distributions decrease from samples MA01 to MA03 to MA02 (**Fig. 3e**). The quartz grain sizes are distributed bimodally in MA03, displaying two distinct peaks at 17 and 96 mm, as is also observed from optical microscopy (**Fig. 3c**). The hematite grains are much finer (< 6 mm), with the coarsest grains (median: 0.78 mm) in MA01. Samples MA02 and MA03 have approximately similar grain sizes with 0.34 and 0.38 mm as the medians, respectively (**Fig. 3f**).

A close inspection of the samples under optical microscope reveals contrasting microstructures across the samples. A large section of MA01 shows equilibrium microstructures within the quartz grains, manifested by well-developed triple junctions and straight grain boundaries (**Fig. 4a**). The individual grains host deformation lamellae (≤ 100 mm long), distributed mostly along the periphery of the grains (**Fig. 4a**). Evidence of bulging recrystallization (BLG) are numerous in MA02 (**Fig. 4b**), along with grain boundary migration recrystallization (GBM), as is revealed by the lobate grain boundaries (**Fig. 4c**). Subgrains are also prominent, with the boundaries being both parallel (**Fig. 4d**) and perpendicular (**Fig. 4e**) to the long axes of the parent grains. Chessboard extinction is rare but present (**Fig. 4f**). The quartz grains in MA03 exhibit similar microstructures as in MA02. The fine-grained domains mostly preserve signatures of BLG and GBM (**Fig. 4g**), whereas the coarser grains exhibit prominent subgrains and weakly developed chessboard microstructure (**Fig. 4h**). We note that unlike **Fig.**

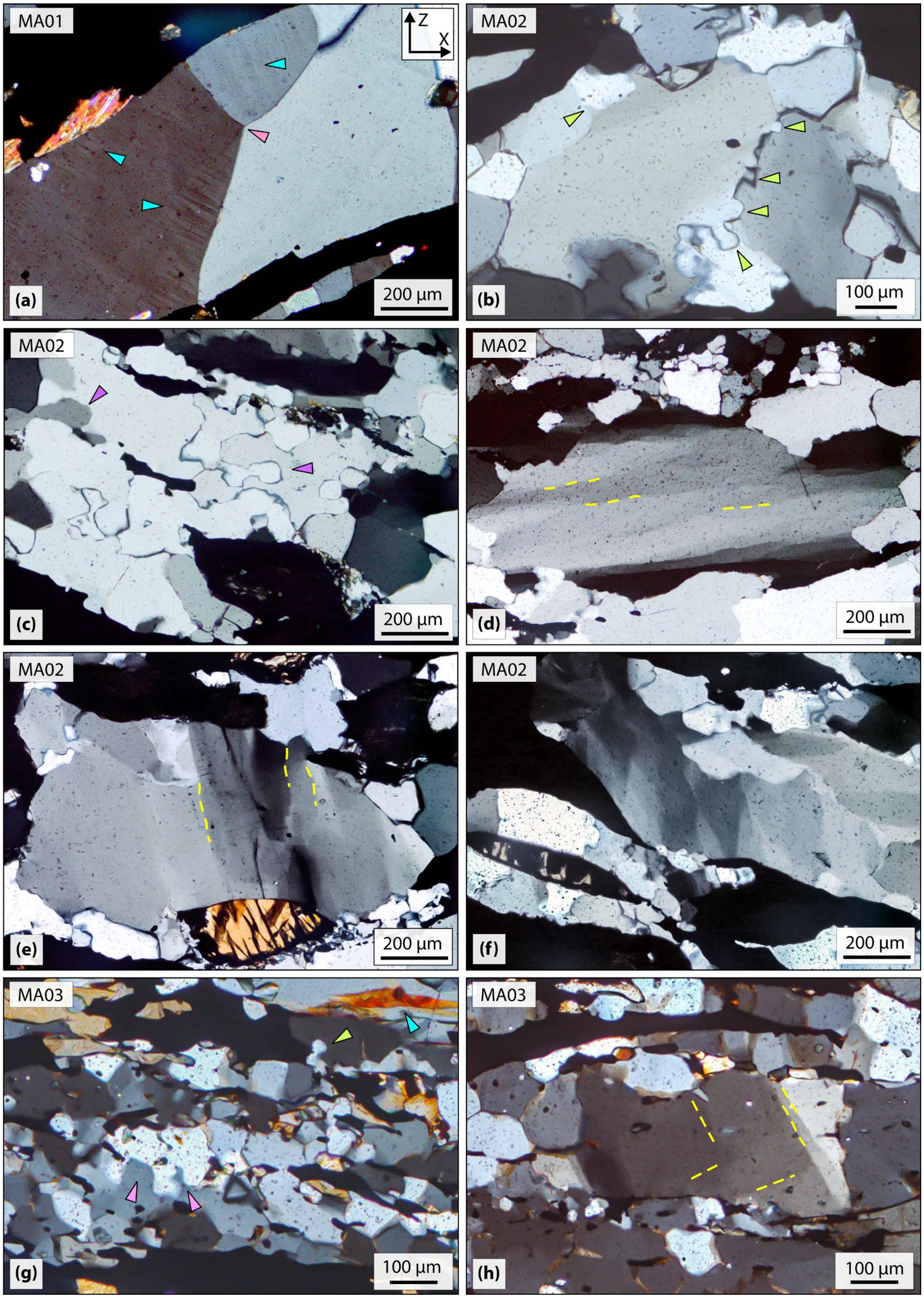

Fig. 4. *Quartz deformation microstructures in the ductile regime.* ***(a)*** *Equant, euhedral and blocky quartz grains with deformation lamellae (blue arrowheads). A triple point junction (pink*

*arrowhead) is also distinct. Evidence of **(b)** bulging recrystallization (bulges marked by green arrowheads) and **(c)** grain boundary migration (purple arrowheads). Subgrain boundaries, both **(d)** parallel and **(e)** perpendicular to the long axes of the grains. **(f)** Chessboard extinction signifying high temperature (>650 °C) deformation. **(g)** Lobate grain boundary (pink arrowheads) and grain bulge (yellow arrowhead) indicating possible recrystallization by GBM and BLG, respectively. A bent orthopyroxene lath with plagioclase is also shown (blue arrowhead). **(h)** Two near-perpendicular subgrain boundaries. Selected portions of the subgrain boundaries in **(d)**, **(e)** and **(f)** have been traced with yellow dashed lines. The kinematic axes for all photomicrographs are oriented as illustrated in **(a)**, except **(e)** and **(f)** where the microscope stage was rotated counterclockwise for a maximum of 15° from the X-direction.*

4b-c and 4g, grain boundary migration (GBM) and bulging (BLG) is less evident in **Fig. 4h**, where both the processes (BLG and GBM) were probably inhibited by the presence of secondary phases (pinning effect).

Overall, the thin section observations and grain size data reveal coarsening of the quartz grains from sample MA02 to MA03 to MA01. Furthermore, we note that the volume of recrystallized quartz grains is relatively higher in both MA02 and MA03 than MA01. In the following sections, we present quantitative analysis of microstructures and textures of quartz, magnetite, and hematite grains of the three samples.

4.2 Crystallographic preferred orientations

The EBSD-derived phase, grain, and orientation maps, from all samples, show intergrowth of the two Fe-oxides as well as the interlayered nature of quartz and magnetite/hematite domains (**Fig. 5**). In MA01, extensive intergrowth of magnetite and hematite has been observed (**Fig. 5a**). The quartz grains in this sample exhibit triple junctions, straight boundaries, and no intracrystalline deformation (**Fig. 5b**). Growth of the hematite grains along the magnetite grain interfaces is evident in MA02 (**Fig. 5c**). Ductile deformation of both magnetite and quartz in MA02 is indicated by the prominent intragranular orientation variations (**Fig. 5c-f**). In MA03, the quartz grains are dynamically recrystallized (**Fig. 5f**).

The quartz grains exhibit well-defined CPOs, and their CPO strengths, measured using the J_{ODF}, M, and mpfJ, are relatively higher for the samples MA01 and MA03 than that of MA02 (**Fig. 6a-c**). The (0001) for both MA01 and MA03 are concentrated close to the Y-axis, whereas

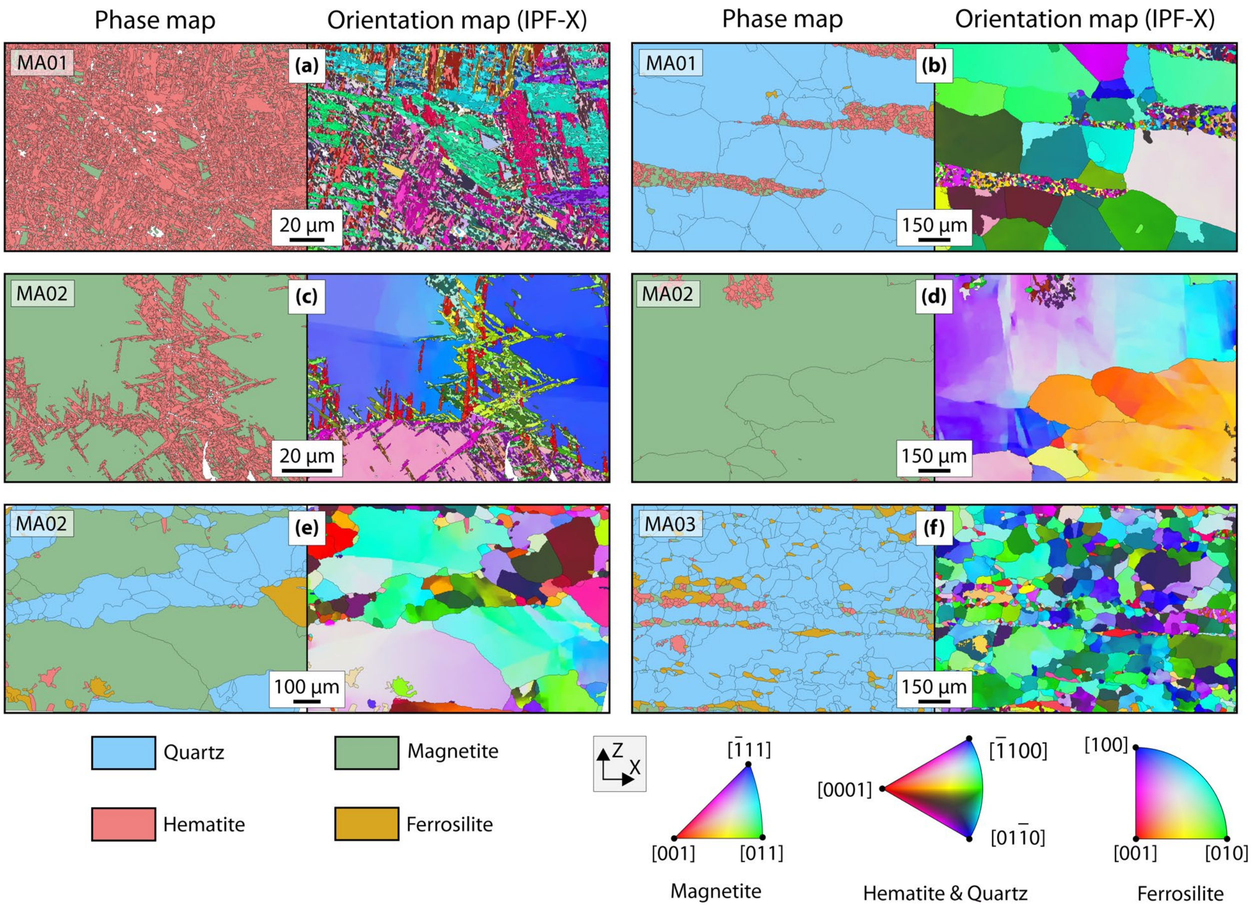

Fig. 5. *Selected EBSD derived phase and orientation (IPF-X) maps. Magnetite-Hematite intergrowth textures are shown in* ***(a)*** *and* ***(c)****, wherein the latter have replaced the former along fractures intersecting at angles 60, 90 or 120°. The layered nature of the quartz and Fe-oxide domains are noticeable in* ***(b)****,* ***(e)*** *and* ***(f)****. However, in* ***(f)*** *the Fe-oxide layers are much thinner. Intracrystalline plastic deformation of magnetite has also been noted in a few grains from sample MA02 as shown in* ***(d)****. All the figures represent XZ-sections. The color codes corresponding to each mineral in the orientation maps are provided at bottom right.*

in MA02, they are dispersed along the periphery of the stereonet. The maxima (yellow squares in **Fig. 6a-c**) for (0001) lie on the YZ-plane for samples MA01 and MA03, whereas, for MA02 it is oblique to both XZ- and YZ-planes. The poles to both (11$\bar{2}$0) and (10$\bar{1}$0) show girdle distributions, and the maxima plot closer to the XY-plane in MA02 than MA01 (**Fig. 6a,b**). Both are parallel to the lineation in MA03 (**Fig. 6c**). The poles to (10$\bar{1}$1) exhibit a weak dispersion around the Y-axis for all the samples, however, the obliquity of the maxima to the XY-plane decreases from MA02 to MA03 to MA01. In the case of MA01, the maximum is nearly parallel to the lineation.

The hematite (**Fig. 6d-f**) and magnetite (**Fig. 6g-i**) grains of all samples exhibit well-developed CPOs. In the case of hematite, the $(10\bar{1}0)$ CPO are the strongest, followed by $(11\bar{2}0)$, $(10\bar{1}1)$, and (0001) as suggested by their respective mpfJ values. For magnetite grains, mpfJ decreases from (110) to (111) and (100). Both J_{ODF} and M for the hematite grains are close for all the samples and lower than those of magnetite. However, the hematite J_{ODF}, derived using all indexed points, in MA02 is higher than that of magnetite. Most of the pole figure maxima (yellow squares in **Fig. 6**) are oblique to the kinematic axes for both hematite and magnetite. The hematite $(10\bar{1}\bar{2})$ maximum is parallel to the Z axis in MA01, and those of (0001) and $(10\bar{1}1)$ lie close to the X and Y axes, respectively, in MA03. The [100] maxima for magnetite in all samples, are at low angles to the XY plane.

Interestingly, for each sample, the CPO distribution of (111) of magnetite grains (**Fig. 6g-i**) matches with those of (0001) of hematite (**Fig. 6d-f**). This geometric relationship is particularly evident in sample MA02, wherein the (0001) of hematite grains are oriented parallel to the (111) of their respective host magnetite grains (**Fig. 7**). Furthermore, the hematite grains have preferably grown along interfaces that are parallel to the traces of the octahedral faces {111} of magnetite grains.

4.3 Misorientation and subgrain boundary trace analysis

The low-angle neighbor-pair misorientation analysis of the quartz grains demonstrates that majority of the subgrain boundaries in all the samples are general, i.e., have both tilt and twist characters, (**Fig. 8a-c**) with the maximum (>90 %) being in MA01 (**Fig. 8a**). The corresponding misorientation axes mostly plot near $[01\bar{1}1]$ and $[01\bar{1}2]$ (**Fig. 8a**). The LAX maxima in both MA02 (**Fig. 8b**) and MA03 (**Fig. 8c**), for all the three subgrain boundary categories, are parallel to the [0001]. In MA03, the LAXs corresponding to the tilt boundaries also exhibit a sub-maximum near $[\bar{1}100]$. The peak of the neighbor-pair MAD at 60° indicates the presence of Dauphine twinning (Tullis, 1970; Barton and Wenk, 2007). Besides, the misfit between the random and theoretical distributions is the highest for MA03, whereas for MA02, they are near similar (**Fig. 8d-f**).

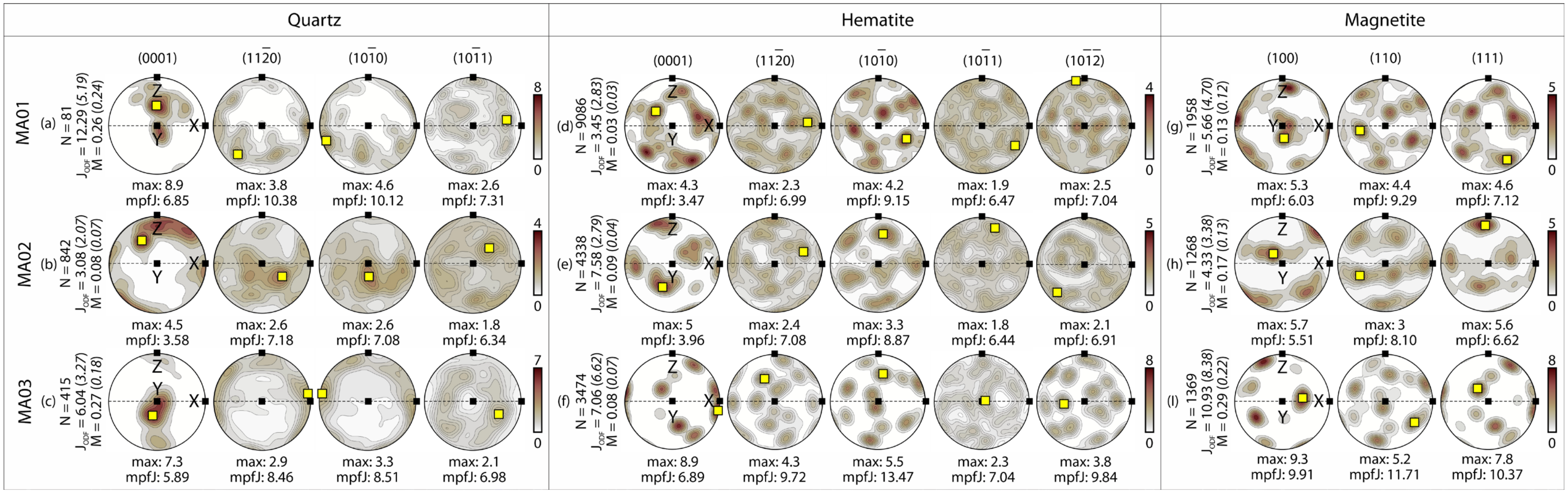

Fig. 6. *Selected pole figures for quartz, hematite, and magnetite grains. Pole figures are derived using one point from each grain. They are equal area, lower hemisphere plots and are contoured to multiples of uniform density (m.u.d). The kinematic axes (X, Y, and Z) for all the pole figures are represented by black squares. Yellow squares show the positions of the density maxima. For each set of CPO plots, the* J_{ODF} *and M, calculated using all the indexed points and one point per grain, are stated outside and within the brackets in italics, respectively. N = number of grains. mpfJ = product of the pole figure intensity and the corresponding multiplicity factor (Mainprice et al., 2015). Color map 'bilbao' (Crameri, 2018) is used here.*

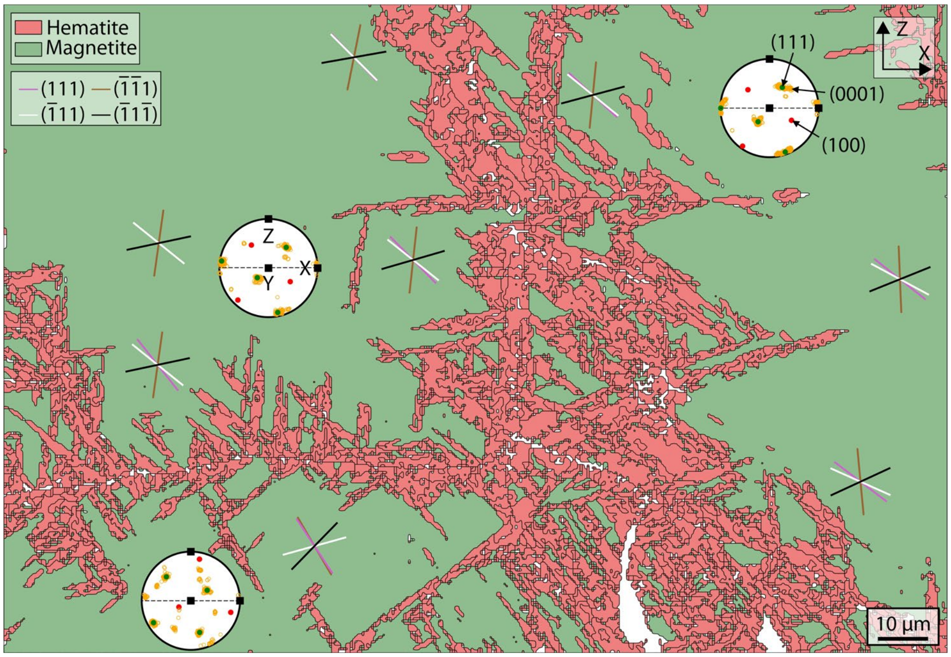

Fig. 7. *Selected grain map from sample MA02, pole figure plots and traces of {111}. The poles to the three symmetrically equivalent planes of (100) (red filled circles) and (111) (green filled circles) of magnetite are plotted along with the poles to (0001) (orange open circles) of hematite grains, following 'one-point-per-grain' method. Each pole figure refers to the magnetite grain upon which it lies, and the corresponding hematite inclusions. The straight lines show the traces of the four symmetrically equivalent planes of {111} of magnetite. These are derived from the orientation data corresponding to the point of intersection of the lines.*

For the magnetite grains as well, the random and theoretical distributions are near similar in MA01 (**Fig. 9a**), but the misfit between the two is higher in both MA02 (**Fig. 9b**) and MA03 (**Fig. 9c**). The MAD for MA01 exhibits a distinct peak at ~60° that corresponds to a rotation about $[\bar{1}11]$ (**Fig. 9d**), as is inferred from the misorientation axis distribution (MXD) plotted on the crystal coordinate system. However, the MAD for MA02 consists of peaks at ~28, ~42, and ~52°, and the corresponding axes of dominantly cluster near $[\bar{1}11]$, [011], and [011]/$[\bar{1}22]$, respectively (**Fig. 9e**). In MA03, the axes for both the peaks in the neighbor-pair MAD at ~30° and ~60° parallel $[\bar{1}11]$ (**Fig. 9f**). Both MAD and MXD for hematite are near identical in all the samples. Therefore, we present the data of MA01, with the highest number of grains, only. The random MAD for hematite differs from that of the theoretical (**Fig. 9g**). The neighbor-pair MAD exhibits notable peaks at ~60, ~70, and a few within 88–92°. The

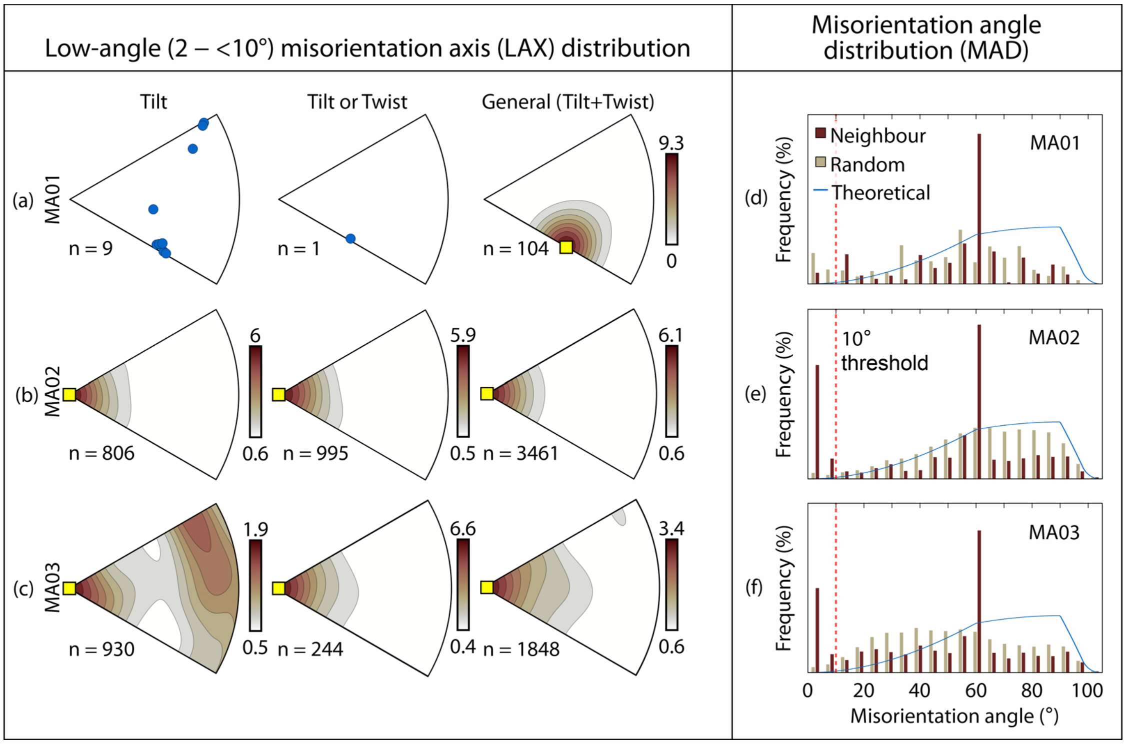

Fig. 8. Quartz misorientation data. ***(a-c)*** *The low-angle (2–10°) 'neighbor pair' misorientation axes (LAXs) for tilt, tilt/twist, and general subgrain boundaries are plotted on the crystal coordinate system (Please refer to Fig. 5 for the crystal reference frame definition). The plots are contoured to multiples of uniform density (m.u.d). Yellow squares show the positions of the density maxima. n = no. of axes. Color map 'bilbao' (Crameri, 2018) is used here.* ***(d-f)*** *Misorientation angle distribution (MAD) histograms for the three samples.*

corresponding HAXs cluster(s) is(are) parallel to [0001], $[01\bar{1}0]$ and $[\bar{1}100]$, and $[\bar{1}2\bar{1}4]$ (**Fig. 9h**). The number of neighbor-pair misorientation angles are also higher than their random-pair counterparts in all the samples for both magnetite and hematite grains (**Fig. 9a-c,g**).

The intragranular deformation of the magnetite grains is evident from the mis2mean, with maxima ranging from 9–41°, and orientation maps (**Figs. 10,11**). One set of selected grains (Grains 1–6, **Fig. 10a-f**) dominantly exhibit tilt subgrain boundaries ($\alpha < 15°$) (**Fig. 10g-l**). Various slip systems are identified from these grains (**Fig. 10m-r**) viz. $(111)[10\bar{1}]$, $(011)[10\bar{1}]$, (001)[110], (011)[110], etc., with the possible operation of more than one slip system in three of them (Grain 1–3, **Fig. 10m-o**). The slip directions of the identified slip systems are symmetrically equivalent to [110], except for Grains 3, 4, and 5, which suggest slip along $[\bar{1}1\bar{1}]$, [100], and

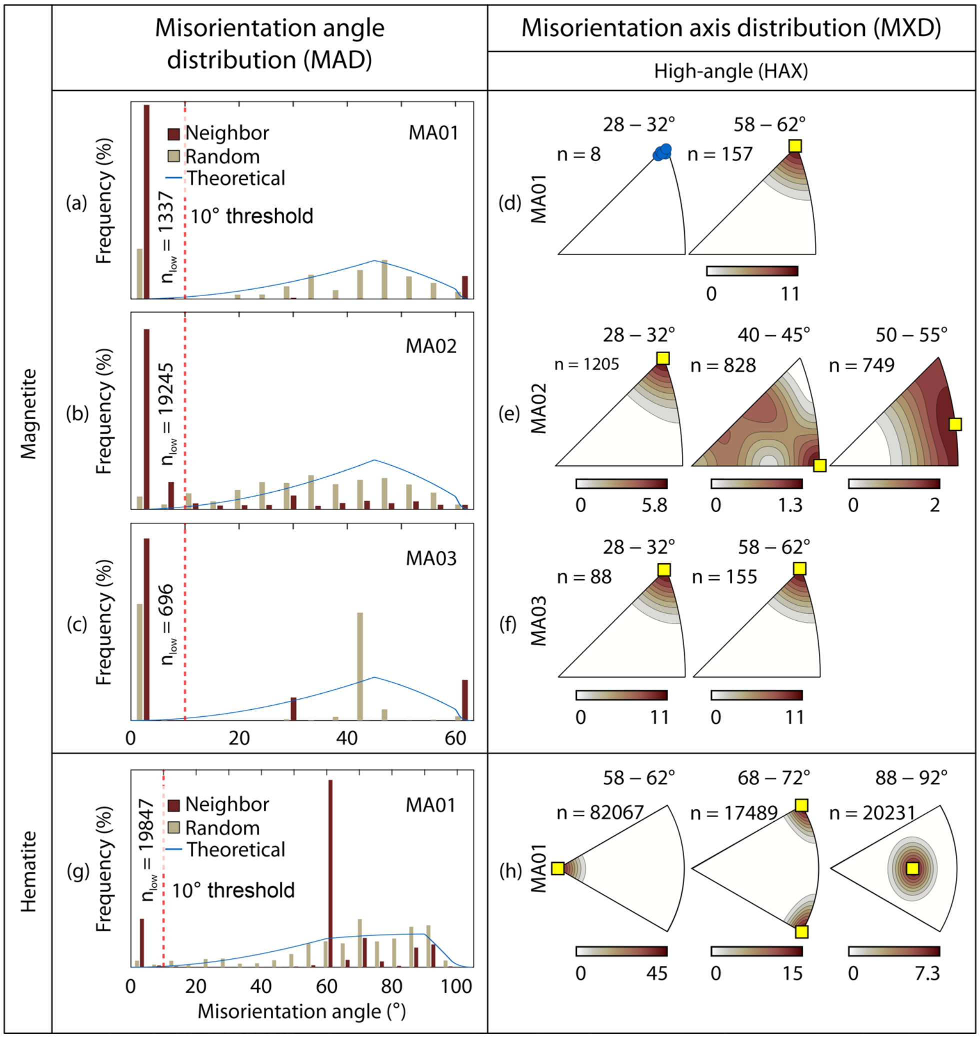

Fig. 9. *Magnetite and hematite misorientation data. The misorientation axes are plotted on the crystal coordinate system (Please refer to Fig. 5 for the crystal reference frame definitions) and are contoured to multiples of uniform density (m.u.d). No misorientation axes were detected for angles >62° in magnetite in **(d)** and **(f)**. Yellow squares show the positions of the density maxima. n = no. of axes. Color map 'bilbao' (Crameri, 2018) is used here. For hematite **(g,h)**, the distributions are near identical for all the three samples and hence only one corresponding to sample MA01 is shown here. n_{low} = no. of low-angle (1–<10°) neighbor-pair boundaries.*

[001], respectively. All the poles to the three slip planes in Grains 3 (**Fig. 10o**) and 6 (**Fig. 10r**) are nearly parallel to ⟨112⟩. The dispersion axes are at low angles (<20°) to the LAX maxima for all the selected boundaries except regions C in Grain 1 (**Fig. 10g,m**), A in Grain 2 (**Fig. 10h,n**), and both A and B in Grain 3 (**Fig. 10i,o**).

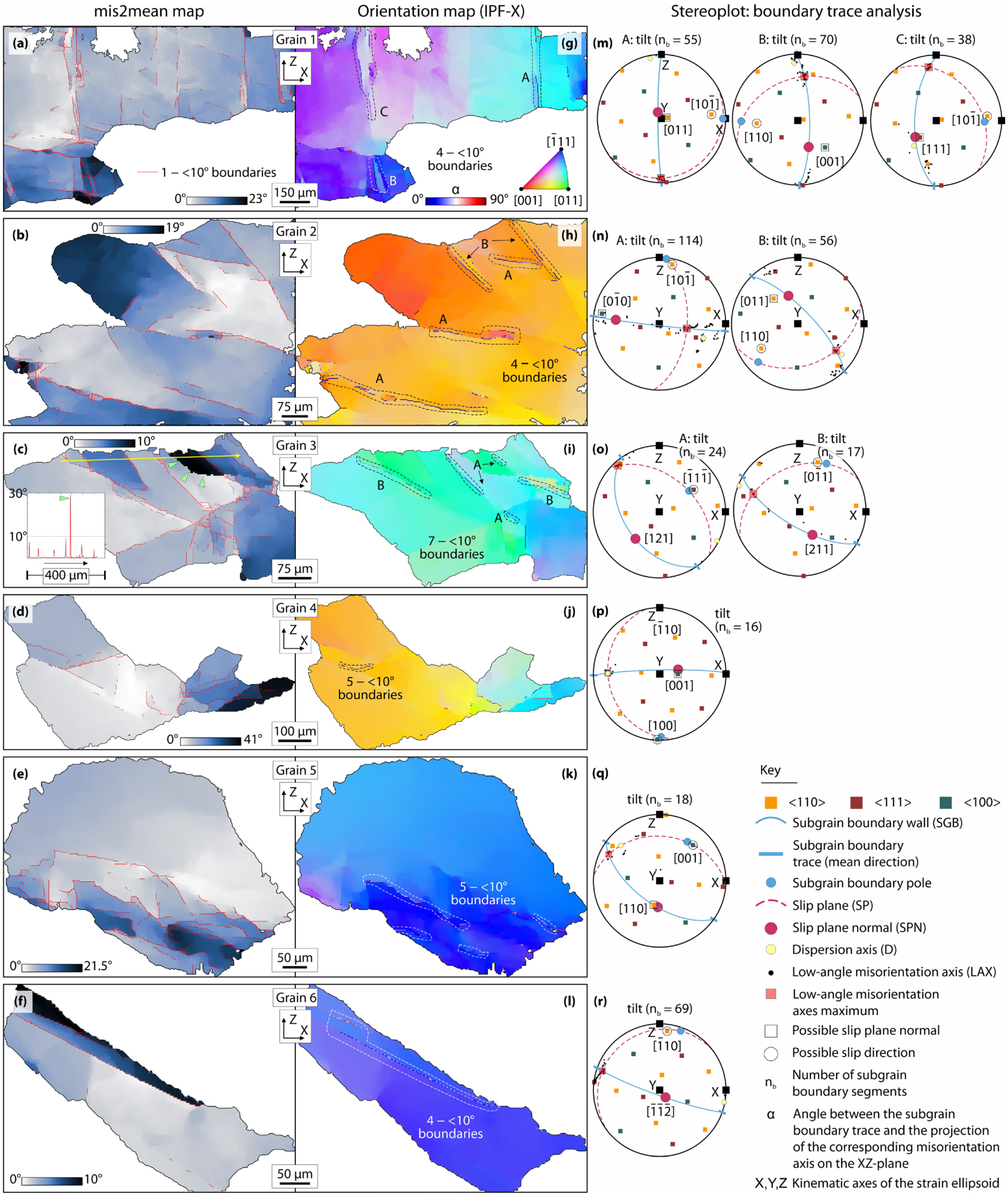

Fig. 10. *Misorientation to mean (mis2mean), orientation maps (IPF-X), and results of the subgrain boundary trace analysis of selected magnetite grains from sample MA02 with tilt boundaries (α < 15°).* ***(a-f)*** *mis2mean maps. The red lines inside each grain in represent subgrain boundaries (1–<10°). The inset plot in* ***(c)*** *shows the 'point-to-point' variation in misorientation along the yellow arrow. The distance (µm) and misorientation angle (°) are plotted along the x-*

and y-axes, respectively. Horizontal dashed line in the plot refers to the minimum threshold for high-angle grain boundaries. The green arrowhead marks the peak corresponding to an isolated intragranular high-angle boundary, which is also pointed out with arrowheads within the grain. The inverted sequence of the scientific colour map 'oslo' (Crameri, 2018) is used in ***(a) - (f)****.* ***(g-l)*** *Orientation maps (IPF-X). The IPF color key for all the grains (1–6) is the same as the one presented in* ***(g)****. The subgrain boundary traces within each grain in the orientation maps are color coded according to their a values and the color bar for all are the same as the one shown in* ***(g)****. The range of misorientation angles, across the subgrain boundaries, vary (Grains 1, 2, and 6 = 4–<10°; Grain 3 = 7–<10°, and Grains 4 and 5 = 5–<10°) and are mentioned for each grain. The analyzed subgrain boundary traces lie within the area enclosed by dashed lines.* ***(m-r)*** *Stereoplots, generated using our script (Supplementary Text S1), illustrating the results of the subgrain boundary trace analysis. The filled orange, brown, and green squares refer to the orientations of ⟨110⟩, ⟨111⟩, and ⟨100⟩ corresponding to the mean orientation (mis2mean value = 0°) of the respective grains.* n_b *= no. of subgrain boundary traces. The black squares represent the X, Y, and Z kinematic axes.*

For the subgrain boundaries of Grains 7 and 8 (**Fig. 11a,b**), $\alpha > 75°$ (**Fig. 11c,d**) and hence they could either be tilt or twist. We have illustrated the stereoplots corresponding to both the possibilities (**Fig. 11e,f**). Twist boundaries are more complex than their tilt counterparts and are associated with two different burgers vectors (Lloyd, 2004). Assuming a twist geometry, we note that both $[10\bar{1}]$ and $[\bar{1}10]$ are (near-) parallel to the estimated slip plane and thus could be the two slip directions, whereas $(\bar{1}12)$ acted as the slip plane (**Fig. 11e**). However, the estimated slip system, assuming a tilt boundary, would be $(11\bar{1})[\bar{1}10]$ (**Fig. 11e**). Similarly, if the subgrain boundaries in Grain 8 were produced by screw or edge dislocations, $(001)[\bar{1}10]$ + (001)[110] or (001)[110] were dominant, respectively. For both the sets of subgrain boundaries, the dispersion axes are parallel to the LAX maxima.

The GOS maps from samples MA02 and MA03 reveal that the hematite grains are relatively more strained than the host magnetite grains (**Fig. 12a-c**). However, >80 % of the grains of both the phases show GOS below 1° (**Fig. 12d-f**).

5. Discussions

The petrographic and microtextural investigations of the three meta-BIF samples revealed possibilities of variation in the deformation intensity, dislocation creep activities in quartz and magnetite, and topotactic replacement of magnetite by hematite. The samples, we

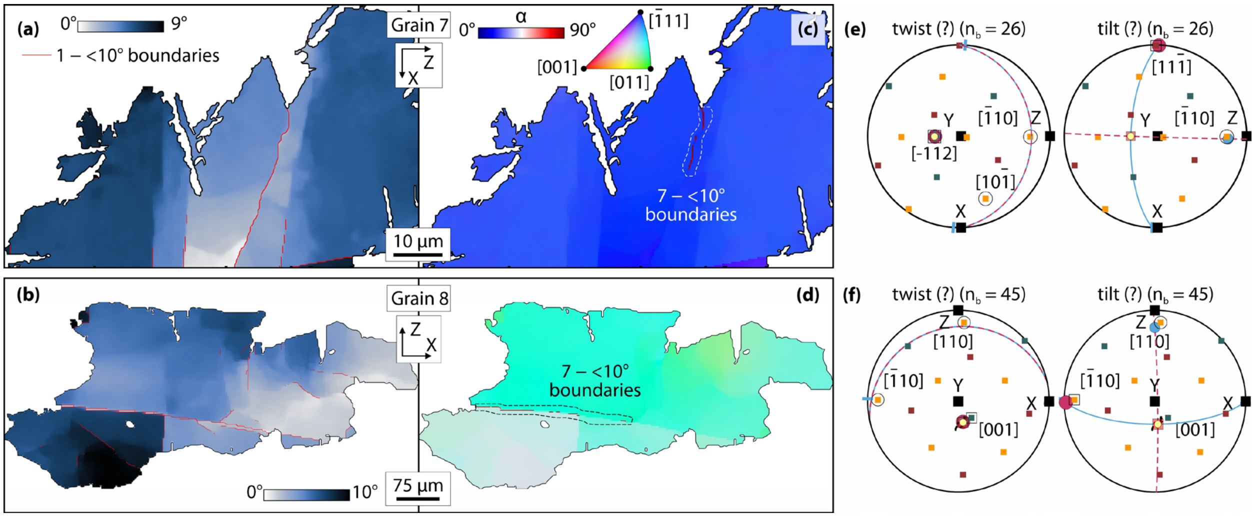

Fig. 11. *Misorientation to mean (mis2mean), orientation maps, and results of the subgrain boundary trace analysis of two magnetite grains from sample MA02 with tilt and/or twist boundaries (α > 75°). The range of misorientation angles, across the subgrain boundaries is 7–<10°. The rest of the description and key are the same as in* ***Fig. 10****.*

studied, represent the presence of deformation/structural heterogeneity over ~40km traverse, which is a significantly small fraction of the entire extent of multiply deformed and metamorphosed CSS. Correlating each of our observations to the overall deformation of CSS would be speculative, and therefore, this study does not attempt the same. Accordingly, the following discussion highlights the intracrystalline deformation mechanisms and textures of the constituent minerals. We first constrain the temperature using plagioclase, orthopyroxene, and quartz microstructures as proxies and then argue the deformation of magnetite and hematite based on the estimated temperature and analyzed EBSD data.

5.1 Deformation of plagioclase and orthopyroxene

Naturally deformed plagioclase exhibits ductile behavior at >500 °C (Allard et al., 2021 & references therein). Laboratory deformation experiments by Mansard et al. (2020), at 800–900 °C and a constant shear strain rate of $10^{-5}s^{-1}$, showed that orthopyroxene + plagioclase aggregates are rheologically weaker than pure plagioclase in the presence of fine-grained reaction products. Moreover, we know that the peak metamorphic grade for the meta-BIF and the interlayered granulites in CSS range from 750 to 800 °C (Talukdar, 2015; Chowdhury and Chakraborty, 2019). Although orthopyroxene + plagioclase reaction products are absent in

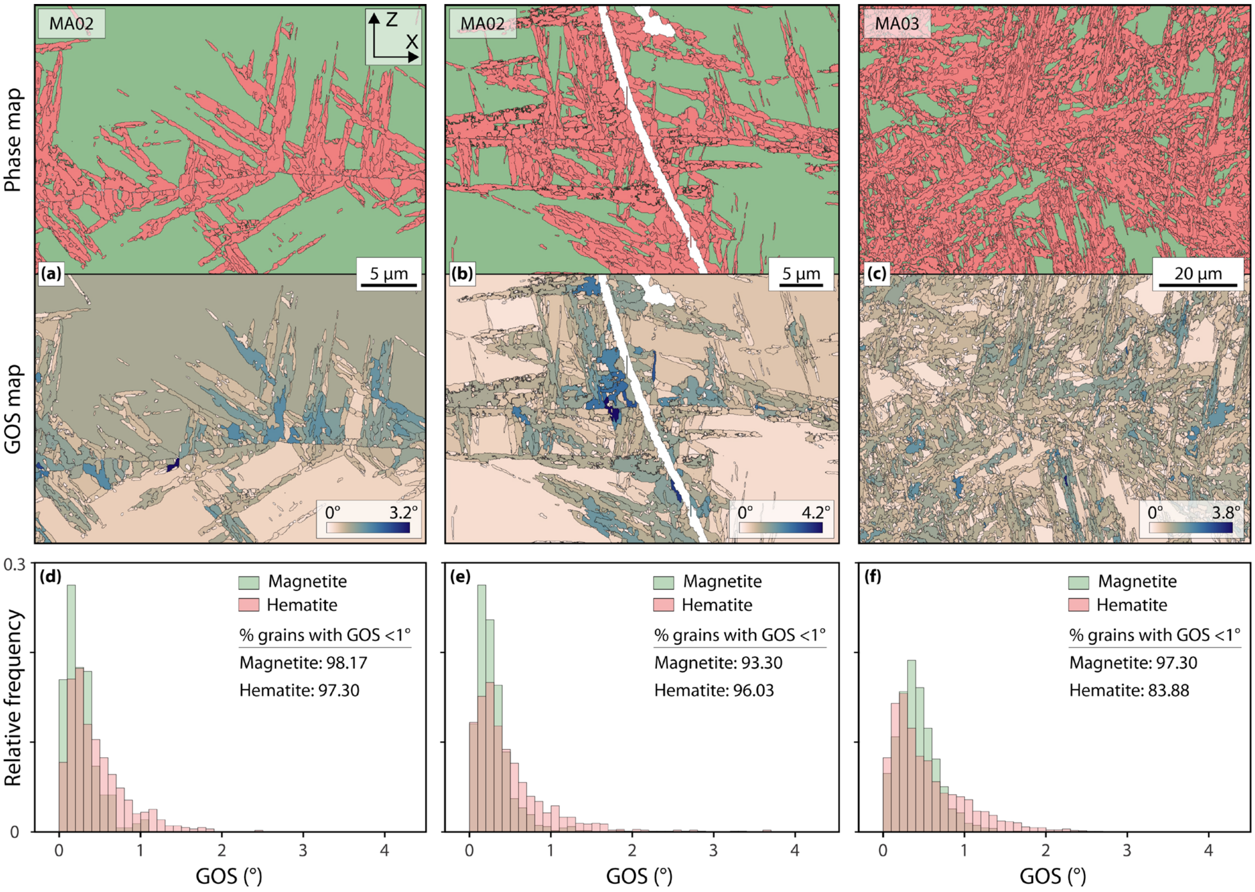

Fig. 12. *Selected phase and grains orientation spread (GOS) maps illustrating the relative variations in intracrystalline deformation between the magnetite and hematite grains.* ***(a-c)*** *Phase map color key is the same as in Fig. 7. The kinematic axes for all the sub-figures are oriented as is shown in* ***(a)****. The inverted sequence of the scientific colour map 'lapaz' (Crameri, 2018) is used in the GOS maps. The histograms in* ***(d)****,* ***(e)****, and* ***(f)*** *show the distribution of the GOS values for both the phases in maps* ***(a)****,* ***(b)****, and* ***(c)****, respectively.*

sample MA03, the plastically deformed orthopyroxene laths inside a plagioclase porphyroclast with bent twin planes (**Fig. 3c** inset) suggests simultaneous ductile deformation of these phases at 500–800 °C. It further signifies that lower strain rates can weaken an orthopyroxene + plagioclase aggregate and trigger ductile behavior below 800 °C, even in the absence of an interconnected network of reaction product(s).

5.2 Deformation of quartz

The quartz microstructures reveal variation in the deformation intensity amongst the samples. Large, equant/blocky and nearly euhedral grains in MA01 (**Figs. 3a** and **4a**) appear to be relatively less deformed than those of both MA02 and MA03, which exhibit finer grains with lobate boundaries and foliation parallel long axes (**Fig. 3b,d)**. In addition to this, the samples also exhibit heterogeneity in the deformation temperature. The presence of deformation lamellae in MA01 indicates low-grade conditions (300–400°C, Passchier and Trouw, 2005). In contrast, quartz deformation microstructures viz. BLG (**Fig. 4b**), SGR (**Fig. 4d,e**), GBM (**Fig. 4c**), and chessboard extinction (**Fig. 4f**) in MA02 and MA03 suggest a wide range of deformation temperatures (280 to ~700 °C) (Kruhl, 1996; Stipp et al., 2002) in the dislocation creep regime (Hirth and Tullis, 1992).

The presence of fine-grained quartz domains on either side of relatively coarser and stretched quartz grains (**Fig. 3c,d**) in MA03 is particularly interesting and could imply, (a) restricted grain growth due to pinning against secondary phase grain boundaries (**Figs. 3d**, **4g,h**) or (b) precursor grainsize heterogeneity. The effect of Zener pinning on grainsize is well known (Herwegh et al., 2011 & references therein) and hence seems applicable to MA03 given the relatively high concentration of fine pyroxene grains (**Fig. 3d**) within the fine-grained quartz domains. Moreover, the possibility of this grain-size variation being a precursor fabric in the BIF could not be refuted.

The distributions of the LAXs, for tilt and tilt/twist boundaries, on the crystal coordinate system were used to infer the dominant slip systems (*Sec. 4.3*). Since general boundaries are composed of both tilt and twist characteristics, which we could not deconvolute, they were avoided from slip system estimation. The orientations of the quartz LAX, corresponding to the tilt boundaries, in both MA02 (**Fig. 8b**, left column) and MA03 (**Fig. 8c**, left column) imply dominance of the{m}⟨a⟩ slip (Neumann, 2000), whereas assumption of twist boundaries (**Fig. 8b,c**, middle column) would suggest simultaneous operation of {c}⟨a⟩ and {c}⟨m⟩ slips (Lloyd, 2004). In MA03, {π}⟨a⟩, and {z}⟨c+a⟩ slip systems were also active (**Fig. 8c**, left column) (Neumann, 2000; Lloyd, 2004). Previous quartz petrofabric studies (e.g., Baëta and Ashbee, 1969; Blumenfeld et al., 1986; Mainprice et al., 1986; Schmid and Casey, 1986) have demonstrated that the common slip systems viz. {m}⟨a⟩, and {c}⟨a⟩ are activated at >450 °C, and 300–400 °C, respectively. Whereas, {c}⟨m⟩ slip is less common and operates at <350 °C (Lloyd and Freeman, 1994; Trimby et al., 1998; Nishikawa and Takeshita, 2000). The LAX orientations clearly suggest that the quartz grains in both MA02 and MA03 were deformed over a wide range of temperature, which is also in agreement with the variety of quartz deformation microstructures observed in the samples.

The quartz CPOs of MA01 (**Fig. 6a**) and MA03 (**Fig. 6c**) show similar strengths, but those of MA02 (**Fig. 6b**) are weaker. The degree of misfit between the theoretical and random pair MADs (**Fig. 8d-f**) concur to this. The relatively weaker CPOs of MA02 (**Fig. 6b**) could be due to the finer grain-size (**Fig. 3e**) (e.g., Rahl and Skemer, 2016). Strong CPOs, despite the euhedral and blocky grains, of MA01 (**Fig. 6a**) suggest that this sample was intensely deformed at earlier stages of its geodynamic evolution, but the grains were statically annealed later such that the CPO was unaffected (Heilbronner and Tullis, 2002). Quartz grains can anneal at temperatures as low as ~350 °C (Trepmann et al., 2010), which lies within the temperature range estimated from the quartz microstructures in MA01 discussed above. Overall, both the presence of non-random CPOs and crystallographically controlled LAXs validate dislocation creep as the dominant mechanism that accommodated intracrystalline deformation (e.g., Baker and Wenk, 1972; Passchier and Trouw, 2005; Díaz Aspiroz et al., 2007; Hunter et al., 2019) in the quartz grains.

To summarize, we suggest that the deformation heterogeneity noted in the quartz grains across the samples might have resulted due to anomalous distribution of temperature. In addition to this, initial grain size variation of the quartz grains also can influence the variation in deformation. The reason behind the temperature gradient in this region has not been explored in this work, however, relative rate of cooling during exhumation could be a possible factor.

5.3 Deformation of magnetite

The magnetite grains of MA01 and MA02 were deformed to similar intensities as is indicated by both the J_{ODF}, M (**Fig. 6g,h**) and the degree of misfit between theoretical and random MADs (**Fig. 9a,b**). Although the clustering of data within a few angular ranges in the

MAD of MA03 (**Fig. 9c**) provides little information about the deformation intensity, J_{ODF} & M (**Fig. 6i**) suggest that the magnetite grains of MA03 are more strained than that of both MA01 and MA02. Nevertheless, the magnetite grains in all the samples exhibit well-developed CPOs (**Fig. 6g-h**) and high frequencies of neighbor-pair low-angle boundaries (**Fig. 9a-c**), both of which imply dislocation creep accommodated ductile deformation (Jiang et al., 2000). The intragranular plastic deformation of magnetite is also evident from the mis2mean maps of selected grains of MA02 (**Figs. 10,11**). Additionally, both MA01 (**Fig. 9a,d**) and MA03 (**Fig. 9c,f**) show the presence of {111} twinning – identified from the ~60° peaks in the neighbor-pair MADs and the corresponding [111] rotation axes (Ferreira et al., 2016; Jacob et al., 2016). This indicates that magnetite continued to deform in ductile regime below 400 °C (Hennig-Michaeli and Siemes, 1975; Agar and Lloyd, 1997).

Laboratory experiments aimed at identifying the possible slip-systems of magnetite reveal $\{111\}\langle110\rangle$ to be the dominant one below 400 °C (Muller and Siemes, 1972; Hennig-Michaeli and Siemes, 1975), whereas, $\{110\}\langle110\rangle$ and $\{100\}\langle110\rangle$ are reported for deformation at 1100 °C (Till and Moskowitz, 2014). Subgrain boundary trace analysis conducted on the selected grains of MA02 confirm slip along {111}, {110}, and {100}, and further testify to dislocation creep activity in magnetite from a naturally deformed sample that has rarely been reported in the literature (e.g.,Boyle et al., 1998; Mamtani et al., 2020). Additionally, we observed that slip parallel to {112} could have operated as well (**Fig. 10o,r**). Although $\langle110\rangle$ is the only slip direction reported for all spinel structured crystals like magnetite (Hornstra, 1960), this study shows that slip along $\langle111\rangle$ (**Fig. 10o**) and $\langle100\rangle$ (**Fig. 10p**) could also be possible in naturally deformed magnetite grains. For both Grains 7 and 8 $\alpha > 75°$, implying that the subgrain boundaries could either be composed of edge or screw dislocations. However, we have observed that the dispersion axes, for both the cases, are nearly parallel (<5°) to the LAXs (**Fig. 11e,f**), suggesting that these are more likely to be tilt boundaries (**Fig. 2a**) (Lloyd, 2004; Hull and Bacon, 2011).

5.4 Topotactic relationship between magnetite and hematite

Replacement/transformation, both redox (Davis et al., 1968; Powell et al., 1999; Taylor et al., 2001; Morris, 2003) and non-redox (Ohmoto, 2003; Otake et al., 2007; Upadhyay et al., 2021; Yin et al., 2022), of magnetite to hematite is a widely researched topic. Both processes entail the inheritance of orientations by the replaced from the host crystals such that the transformation is characterized by one or more crystallographic relations (Barbosa and Lagoeiro, 2010; Barbosa et al., 2020; Braga de Oliveira et al., 2020; Yin et al., 2022). The most widely reported topotaxial relationship, parallelism of the (0001) of hematite to the (111) of magnetite grains, is associated with redox transformations. Whereas, recently conducted nanoscale study of BIF samples from the East Kunlun Orogenic Belt (N Tibet) by Yin et al. (2022), demonstrated that redox independent transformations could cause ($10\bar{1}\bar{2}$) of hematite to grow parallel to (110) of the magnetite grains.

The crystallographic orientations of magnetite (**Fig. 6g-i**) and hematite (**Fig. 6d-f**) grains obtained from the meta-BIF samples show that the maxima for [111] in magnetite and [0001] in hematite are indeed parallel. The same is further demonstrated from a single EBSD scan in **Fig. 7** where all the (111) of the host magnetite grains overlie the (0001) of the replaced hematite grains. We also noticed a similar relation between [110] of magnetite and hematite ($10\bar{1}0$) (**Fig. 6d-i**). However, parallelism between [110] of magnetite and ($10\bar{1}\bar{2}$) of hematite is absent (**Fig. 6d-i**) implying that the topotaxial replacement occurred via a redox reaction. The peak of neighbor-pair MAD at ~60° for hematite corresponds to [0001] rotation axis, and this feature has been inherited from the host magnetite grains that exhibit 60° rotation about [111].

Lagoeiro (1998) had proposed that hematite grains that replace the host magnetite are dislocation-free and thus weaker. This study suggests that the post-replacement deformation, if any, was weak. Consequently, the hematite CPOs, inherited from the strongly deformed (pre-replacement) magnetite grains, were unaffected and exhibit lower J_{ODF} and M-index values than their hosts despite their oriented growth (**Fig. 7**). The low GOS values (**Fig. 12**) displayed by >80% of the grains of both magnetite and hematite along with the well-developed CPOs indicate that recovery processes, which also produced the subgrain boundaries (**Fig. 9a-c,g**), were rapid and hence did not influence the deformation induced crystallographic fabric (e.g. Gomez-Rivas et al., 2017).

6. Conclusions

Three meta-BIF samples (MA01, MA02 and MA03), collected from the Cauvery Shear System (CSS) of Southern Granulite Terrane in India have been examined in this work with a particular focus on their microstructural characteristics. The samples comprise of mostly quartz, magnetite and hematite with plagioclase and pyroxenes as accessories. The quartz grain size strongly varies among the samples and in one of them (MA03) the grain size distribution is bimodal, which could either be a precursor fabric or a product of Zenner pinning. Microstructural features viz. BLG, SGR, GBM recrystallization in quartz are dominant in MA02 and MA03, However, sample MA01 shows annealed microstructures and has the coarsest grains. The quartz CPOs are relatively stronger in both MA01 and MA03 than MA02. Both the quartz microstructures and EBSD-derived data suggest that the samples were deformed under various temperature ranges and the deformation was dominantly accommodated by dislocation creep. The magnetite grains exhibit subgrains and strong CPOs, both of which testify to dislocation creep accommodated deformation. Furthermore, the presence of {111} twinning suggests ductile deformation of the magnetite grains even below 400 °C, which resulted in the activation of the {111}⟨110⟩ slip system. Subgrain boundary trace analysis of magnetite also hints activation of {111}, {110}, {100}, and possibly {112} as slip planes, with the possible operation of multiple slip systems. Redox topotaxial replacement, of the magnetite grains by hematite, characterized by the parallelism of the hematite (0001) to magnetite (111), has been observed in all the samples. This replacement has preferentially occurred parallel to the traces of {111} of the magnetite grains, causing oriented deposition of the hematite grains. The well-developed CPOs along with low (<1°) GOS values suggest that the recovery processes were fast. We also propose that any post-replacement deformation was weak such that the inherited CPOs of the hematite grains were unaffected. However, the CPO strength indices (J_{ODF} and M) of magnetite are higher than hematite and possibly reflect the relatively strong pre-replacement deformation.

Acknowledgements

Department of Earth Sciences and Advanced Center for Material Sciences (ACMS) of IIT Kanpur supported the sample preparation and EBSD data acquisition, respectively. We thank Sarvesh Swamy for helping us during the EBSD data acquisition. Discussions on tilt and twist boundaries with Zachary Michels and on the BIFs with Pulak Sengupta and Moumita Talukdar improved the quality of the manuscript. Anshika Singh and Arindam Sarkar assisted initially in preparing the samples. DD acknowledges an Institute Postdoctoral Fellowship awarded to him by IIT Kanpur. This work is supported by a Swarnajayanti Fellowship (DST/SJF/E&ASA-01/2015-16) awarded to SM. We thank Mark Pearce and an anonymous reviewer for critically reviewing the manuscript and Virginia Toy for editorial handling.

Data Statement

The EBSD data used in this study can be obtained from the Mendeley Data Repository (DOI: 10.17632/hcwtns8d47.2).

References

Agar, S.M., Lloyd, G.E., 1997. Deformation of Fe-Ti oxides in gabbroicshear zones from the MARK area, Proceedings of the Ocean Drilling Program, Scientific Results. Ocean Drilling Program. https://doi.org/10.2973/odp.proc.sr.153.1997

Allard, M., Ildefonse, B., Oliot, É., Barou, F., 2021. Plastic Deformation of Plagioclase in Oceanic Gabbro Accreted at a Slow-Spreading Ridge (Hole U1473A, Atlantis Bank, Southwest Indian Ridge). Journal of Geophysical Research: Solid Earth 126. https://doi.org/10.1029/2021JB021964

Bachmann, F., Hielscher, R., Schaeben, H., 2011. Grain detection from 2d and 3d EBSD data—Specification of the MTEX algorithm. Ultramicroscopy 111, 1720–1733. https://doi.org/10.1016/j.ultramic.2011.08.002

Bachmann, F., Hielscher, R., Schaeben, H., 2010. Texture Analysis with MTEX – Free and Open Source Software Toolbox. Solid State Phenomena 160, 63–68. https://doi.org/10.4028/www.scientific.net/SSP.160.63

Baëta, R.D., Ashbee, K.H.G., 1969. Slip systems in quartz: I. Experiments. American Mineralogist 54, 1551–1573.

Baker, D.W., Wenk, H.-R., 1972. Preferred Orientation in a Low-Symmetry Quartz Mylonite. The Journal of Geology 80, 81–105. https://doi.org/10.1086/627714

Barbosa, P., Lagoeiro, L., Mota e Nogueira, V., 2020. Misorientation relationships in goethite, hematite and magnetite: a case study of iron-formation rocks from the Iron Quadrangle, Brazil. Journal of Applied Crystallography 53, 1334–1342. https://doi.org/10.1107/S1600576720010596

Barbosa, P.F., Lagoeiro, L., 2010. Crystallographic texture of the magnetite-hematite transformation: Evidence for topotactic relationships in natural samples from Quadrilatero Ferrifero, Brazil. American Mineralogist 95, 118–125. https://doi.org/10.2138/am.2010.3201

Barton, N.R., Wenk, H.-R., 2007. Dauphiné twinning in polycrystalline quartz. Modelling and Simulation in Materials Science and Engineering 15, 369–384. https://doi.org/10.1088/0965-0393/15/3/013

Blumenfeld, P., Mainprice, D., Bouchez, J.L., 1986. C-slip in quartz from subsolidus deformed granite. Tectonophysics 127, 97–115. https://doi.org/10.1016/0040-1951(86)90081-8

Boyle, A.P., Prior, D.J., Banham, M.H., Timms, N.E., 1998. Plastic deformation of metamorphic pyrite: new evidence from electron-backscatter diffraction and forescatter orientation-contrast imaging. Mineralium Deposita 34, 71–81. https://doi.org/10.1007/s001260050186

Braga de Oliveira, F., Álvares da Silva, G., Graça, L.M., 2020. Defining the hematite topotaxial crystal growth in magnetite–hematite phase transformation. Journal of Applied Crystallography 53, 896–903. https://doi.org/10.1107/S1600576720006305

Brandt, S., Raith, M.M., Schenk, V., Sengupta, P., Srikantappa, C., Gerdes, A., 2014. Crustal evolution of the Southern Granulite Terrane, south India: New geochronological and geochemical data for felsic orthogneisses and granites. Precambrian Research 246, 91–122. https://doi.org/10.1016/j.precamres.2014.01.007

Bunge, H.-J., 1982. Texture Analysis in Materials Science: Mathematical Methods. Butterworth-Heinemann, Butterworths, London.

Cannat, M., 1991. Plastic deformation at an oceanic spreading ridge: A microstructural study of the Site 735 gabbros (Southwest Indian Ocean). Proceedings of the Ocean Drilling Program, Scientific Results 118, 399–408.

Chernak, L.J., Hirth, G., Selverstone, J., Tullis, J., 2009. Effect of aqueous and carbonic fluids on the dislocation creep strength of quartz. Journal of Geophysical Research 114, B04201. https://doi.org/10.1029/2008JB005884

Chetty, T.R.K., Rao, Y.B., 2006. The Cauvery shear zone, Southern Granulite Terrain, India: a crustal-scale flower structure. Gondwana Research 10, 77–85.

Chowdhury, P., Chakraborty, S., 2019. Slow Cooling at Higher Temperatures Recorded within High- *P* Mafic Granulites from the Southern Granulite Terrain, India: Implications for the Presence and Style of Plate Tectonics near the Archean–Proterozoic Boundary. Journal of Petrology 60, 441–486. https://doi.org/10.1093/petrology/egz001

Chowdhury, P., Talukdar, M., Sengupta, P., Sanyal, S., Mukhopadhyay, D., 2013. Controls of P-T path and element mobility on the formation of corundum pseudomorphs in Paleoproterozoic high-pressure anorthosite from Sittampundi, Tamil Nadu, India. American Mineralogist 98, 1725–1737. https://doi.org/10.2138/am.2013.4350

Collins, A.S., Clark, C., Sajeev, K., Santosh, M., Kelsey, D.E., Hand, M., 2007. Passage through India: the Mozambique Ocean suture, high-pressure granulites and the Palghat-Cauvery shear zone system. Terra Nova 19, 141–147. https://doi.org/10.1111/j.1365-3121.2007.00729.x

Davis, B.L., Rapp, G., Walawender, M.J., 1968. Fabric and structural characteristics of the martitization process. American Journal of Science 266, 482–496. https://doi.org/10.2475/ajs.266.6.482

Díaz Aspiroz, M., Lloyd, G.E., Fernández, C., 2007. Development of lattice preferred orientation in clinoamphiboles deformed under low-pressure metamorphic conditions. A SEM/EBSD study of metabasites from the Aracena metamorphic belt (SW Spain). Journal of Structural Geology 29, 629–645. https://doi.org/10.1016/j.jsg.2006.10.010

Dutta, D., Mukherjee, S., 2019. Opposite shear senses: Geneses, global occurrences, numerical simulations and a case study from the Indian western Himalaya. Journal of Structural Geology 126, 357–392. https://doi.org/10.1016/j.jsg.2019.05.008

Ferreira, F., Lagoeiro, L., Morales, L.F.G., Oliveira, C.G. de, Barbosa, P., Ávila, C., Cavalcante, G.C.G., 2016. Texture development during progressive deformation of hematite aggregates: Constraints from VPSC models and naturally deformed iron oxides from

Minas Gerais, Brazil. Journal of Structural Geology 90, 111–127. https://doi.org/10.1016/j.jsg.2016.07.009

Geological Survey of India, 1995. Geological and mineral map of Tamil Nadu & Pondicherry on 1: 50,000 scale. Geological Survey of India.

Ghosh, J.G., Wit, M.J. de, Zartman, R.E., 2004. Age and tectonic evolution of Neoproterozoic ductile shear zones in the Southern Granulite Terrain of India, with implications for Gondwana studies. Tectonics 23. https://doi.org/10.1029/2002TC001444

Gomez-Rivas, E., Griera, A., Llorens, M.-G., Bons, P.D., Lebensohn, R.A., Piazolo, S., 2017. Subgrain Rotation Recrystallization During Shearing: Insights From Full-Field Numerical Simulations of Halite Polycrystals: Recrystallization during halite shearing. Journal of Geophysical Research: Solid Earth 122, 8810–8827. https://doi.org/10.1002/2017JB014508

Gonçalves, C.C., Gonçalves, L., Hirth, G., 2015. The effects of quartz recrystallization and reaction on weak phase interconnection, strain localization and evolution of microstructure. Journal of Structural Geology, Special Issue: Deformation of the Lithosphere -How Small Structures Tell a Big Story 71, 24–40. https://doi.org/10.1016/j.jsg.2014.11.010

Heilbronner, R., Tullis, J., 2002. The effect of static annealing on microstructures and crystallographic preferred orientations of quartzites experimentally deformed in axial compression and shear. In: De Meer, S., Drury, M.R., De Bresser, J.H.P., Pennock, G.M. (Eds.), Geological Society, London, Special Publications, Deformation Mechanisms, Rheology and Tectonics: Current Status and Future Perspectives 200, 191–218. https://doi.org/10.1144/GSL.SP.2001.200.01.12

Hennig-Michaeli, C., 1977. Microscopic structure studies of experimentally and naturally deformed hematite ores. Tectonophysics, Fabrics, Microstructures, and Microtectonics 39, 255–271. https://doi.org/10.1016/0040-1951(77)90099-3

Hennig-Michaeli, C., Siemes, H., 1975. Zwillungsgleitung beim Magnetite. Neues Jahrbuch Für Mineralogie - Abhandlungen 123, 330–334.

Herwegh, M., Linckens, J., Ebert, A., Berger, A., Brodhag, S.H., 2011. The role of second phases for controlling microstructural evolution in polymineralic rocks: A review. Journal of Structural Geology 33, 1728–1750. https://doi.org/10.1016/j.jsg.2011.08.011

Hielscher, R., Schaeben, H., 2008. A novel pole figure inversion method: specification of the *MTEX* algorithm. Journal of Applied Crystallography 41, 1024–1037. https://doi.org/10.1107/S0021889808030112

Hirth, G., Tullis, J.A.N., 1992. Dislocation creep regimes in quartz aggregates. Journal of Structural Geology 14, 145–159.

Hornstra, J., 1960. Dislocations, stacking faults and twins in the spinel structure. Journal of Physics and Chemistry of Solids 15, 311–323. https://doi.org/10.1016/0022-3697(60)90254-7

Hull, D., Bacon, D.J., 2011. Introduction to dislocations, 5th ed. Butterworth Heinemann, Elsevier, Amsterdam Heidelberg.

Hunter, N.J.R., Weinberg, R.F., Wilson, C.J.L., Luzin, V., Misra, S., 2019. Quartz deformation across interlayered monomineralic and polymineralic rocks: A comparative analysis. Journal of Structural Geology 119, 118–134. https://doi.org/10.1016/j.jsg.2018.12.005

Jacob, D.E., Piazolo, S., Schreiber, A., Trimby, P., 2016. Redox-freezing and nucleation of diamond via magnetite formation in the Earth's mantle. Nature Communications 7, 11891. https://doi.org/10.1038/ncomms11891

Jiang, Z., Prior, D.J., Wheeler, J., 2000. Albite crystallographic preferred orientation and grain misorientation distribution in a low-grade mylonite: implications for granular flow. Journal of Structural Geology 22, 1663–1674. https://doi.org/10.1016/S0191-8141(00)00079-1

Karmakar, S., Mukherjee, S., Sanyal, S., Sengupta, P., 2017. Origin of peraluminous minerals (corundum, spinel, and sapphirine) in a highly calcic anorthosite from the Sittampundi Layered Complex, Tamil Nadu, India. Contributions to Mineralogy and Petrology 172, 67. https://doi.org/10.1007/s00410-017-1383-8

Klein, C., 2005. Some Precambrian banded iron-formations (BIFs) from around the world: Their age, geologic setting, mineralogy, metamorphism, geochemistry, and origins. American Mineralogist 90, 1473–1499. https://doi.org/10.2138/am.2005.1871

Kruhl, J.H., 1996. Prism- and basal-plane parallel subgrain boundaries in quartz: a microstructural geothermobarometer. Journal of Metamorphic Geology 14, 581–589. https://doi.org/10.1046/j.1525-1314.1996.00413.x

Lagoeiro, L.E., 1998. Transformation of magnetite to hematite and its influence on the dissolution of iron oxide minerals. Journal of Metamorphic Geology 16, 415–423. https://doi.org/10.1111/j.1525-1314.1998.00144.x

Lloyd, G.E., 2004. Microstructural evolution in a mylonitic quartz simple shear zone: the significant roles of dauphine twinning and misorientation. Geological Society, London, Special Publications 224, 39–61. https://doi.org/10.1144/GSL.SP.2004.224.01.04

Lloyd, G.E., Freeman, B., 1994. Dynamic recrystallization of quartz under greenschist conditions. Journal of Structural Geology 16, 867–881. https://doi.org/10.1016/0191-8141(94)90151-1

Mainprice, D., Bouchez, J.-L., Blumenfeld, P., Tubià, J.M., 1986. Dominant c slip in naturally deformed quartz: Implications for dramatic plastic softening at high temperature. Geology 14, 819. https://doi.org/10.1130/0091-7613(1986)14<819:DCSIND>2.0.CO;2

Mamtani, M.A., Reznik, B., Kontny, A., 2020. Intracrystalline deformation and nanotectonic processes in magnetite from a naturally deformed rock. Journal of Structural Geology 135, 104045. https://doi.org/10.1016/j.jsg.2020.104045

Mansard, N., Stünitz, H., Raimbourg, H., Précigout, J., 2020. The role of deformation-reaction interactions to localize strain in polymineralic rocks: Insights from experimentally deformed plagioclase-pyroxene assemblages. Journal of Structural Geology 134, 104008. https://doi.org/10.1016/j.jsg.2020.104008

Meißner, B., Deters, P., Srikantappa, C., Köhler, H., 2002. Geochronological evolution of the Moyar, Bhavani and Palghat shear zones of southern India: implications for east Gondwana correlations. Precambrian Research 114, 149–175. https://doi.org/10.1016/S0301-9268(01)00222-4

Michels, Z.D., Kruckenberg, S.C., Davis, J.R., Tikoff, B., 2015. Determining vorticity axes from grain-scale dispersion of crystallographic orientations. Geology 43, 803–806. https://doi.org/10.1130/G36868.1

Morris, R.C., 2003. Iron ore genesis and post-ore metasomatism at Mount Tom Price. Applied Earth Science 112, 56–67. https://doi.org/10.1179/037174503225011216

Mukhopadhyay, J., 2020. Archean banded iron formations of India. Earth-Science Reviews 201, 102927. https://doi.org/10.1016/j.earscirev.2019.102927

Muller, P., Siemes, H., 1972. Zur Festigkeit und Gefügeregelung von experimentel verformten Magnetitersen. Neues Jahrbuch Für Mineralogie - Abhandlungen 117, 39–60.

Neumann, B., 2000. Texture development of recrystallised quartz polycrystals unravelled by orientation and misorientation characteristics. Journal of Structural Geology 22, 1695–1711. https://doi.org/10.1016/S0191-8141(00)00060-2

Nishikawa, O., Takeshita, T., 2000. Progressive lattice misorientation and microstructural development in quartz veins deformed under subgreenschist conditions. Journal of Structural Geology 22, 259–276. https://doi.org/10.1016/S0191-8141(99)00147-9

Noack, N.M., Kleinschrodt, R., Kirchenbaur, M., Fonseca, R.O.C., Münker, C., 2013. Lu–Hf isotope evidence for Paleoproterozoic metamorphism and deformation of Archean oceanic crust along the Dharwar Craton margin, southern India. Precambrian Research 233, 206–222. https://doi.org/10.1016/j.precamres.2013.04.018

Ohmoto, H., 2003. Nonredox transformations of magnetite-hematite in hydrothermal systems. Economic Geology 98, 157–161. https://doi.org/10.2113/gsecongeo.98.1.157

Otake, T., Wesolowski, D.J., Anovitz, L.M., Allard, L.F., Ohmoto, H., 2007. Experimental evidence for non-redox transformations between magnetite and hematite under H2-rich hydrothermal conditions. Earth and Planetary Science Letters 257, 60–70. https://doi.org/10.1016/j.epsl.2007.02.022

Passchier, C.W., Trouw, R.A.J., 2005. Microtectonics, 2nd ed. Springer, Berlin, Heidelberg.

Plavsa, D., Collins, A.S., Foden, J.D., Clark, C., 2015. The evolution of a Gondwanan collisional orogen: A structural and geochronological appraisal from the Southern Granulite Terrane, South India. Tectonics 34, 820–857. https://doi.org/10.1002/2014TC003706

Powell, C.McA., Oliver, N.H.S., Li, Z.-X., Martin, D.McB., Ronaszeki, J., 1999. Synorogenic hydrothermal origin for giant Hamersley iron oxide ore bodies. Geology 27, 175. https://doi.org/10.1130/0091-7613(1999)027<0175:SHOFGH>2.3.CO;2

Prior, 1999. Problems in determining the misorientation axes, for small angular misorientations, using electron backscatter diffraction in the SEM. Journal of Microscopy 195, 217–225. https://doi.org/10.1046/j.1365-2818.1999.00572.x

Prior, D.J., Wheeler, J., Peruzzo, L., Spiess, R., Storey, C., 2002. Some garnet microstructures: an illustration of the potential of orientation maps and misorientation analysis in microstructural studies. Journal of Structural Geology 24, 999–1011. https://doi.org/10.1016/S0191-8141(01)00087-6

Rahl, J.M., Skemer, P., 2016. Microstructural evolution and rheology of quartz in a mid-crustal shear zone. Tectonophysics 680, 129–139. https://doi.org/10.1016/j.tecto.2016.05.022

Ramakrishnan, M., Vaidyanadhan, R., 2008. Geology of India. Geological Society of India, Bangalore, India 1, 556.

Reddy, S.M., Buchan, C., 2005. Constraining kinematic rotation axes in high-strain zones: a potential microstructural method? Geological Society, London, Special Publications 243, 1–10. https://doi.org/10.1144/GSL.SP.2005.243.01.02

Reddy, S.M., Timms, N.E., Pantleon, W., Trimby, P., 2007. Quantitative characterization of plastic deformation of zircon and geological implications. Contributions to Mineralogy and Petrology 153, 625–645. https://doi.org/10.1007/s00410-006-0174-4

Rosière, C.A., Siemes, H., Quade, H., Brokmeier, H.-G., Jansen, E.M., 2001. Microstructures, textures and deformation mechanisms in hematite. Journal of Structural Geology 23, 1429–1440. https://doi.org/10.1016/S0191-8141(01)00009-8

Schmid, S.M., Casey, M., 1986. Complete fabric analysis of some commonly observed quartz C-axis patterns. In: Hobbs, B.E., Heard, H.C. (Eds.), Geophysical Monograph Series. American Geophysical Union, Washington, D. C., 263–286. https://doi.org/10.1029/GM036p0263

Siemes, H., Klingenberg, B., Rybacki, E., Naumann, M., Schäfer, W., Jansen, E., Kunze, K., 2008. Glide systems of hematite single crystals in deformation experiments. Ore Geology Reviews 33, 255–279. https://doi.org/10.1016/j.oregeorev.2006.03.007

Siemes, H., Klingenberg, B., Rybacki, E., Naumann, M., Schäfer, W., Jansen, E., Rosière, C.A., 2003. Texture, microstructure, and strength of hematite ores experimentally deformed in the temperature range 600–1100 °C and at strain rates between 10−4 and 10−6s−1. Journal of Structural Geology 25, 1371–1391. https://doi.org/10.1016/S0191-8141(02)00184-0

Skemer, P., Katayama, I., Jiang, Z., Karato, S., 2005. The misorientation index: Development of a new method for calculating the strength of lattice-preferred orientation. Tectonophysics 411, 157–167. https://doi.org/10.1016/j.tecto.2005.08.023

Stipp, M., Stünitz, H., Heilbronner, R., Schmid, S.M., 2002. The eastern Tonale fault zone: a ‘natural laboratory’ for crystal plastic deformation of quartz over a temperature range from 250 to 700°C. Journal of Structural Geology 24, 1861–1884. https://doi.org/10.1016/S0191-8141(02)00035-4

Subramanian, K.S., Selvan, T.A., 2001. Geology of Tamil Nadu and Pondicherry. Geological Society of India 192.

Talukdar, M., 2015. Metamorphic evolution of some layered magmatic complexes from parts of the Southern Granulite Terrane, Tamil Nadu, India. PhD Thesis. Jadavpur University.

Talukdar, M., Mukhopadhyay, D., Sanyal, S., Sengupta, P., 2020. Early Palaeoproterozoic structural reconstitution of a suite of rocks from the Mahadevi Layered Complex, Tamil Nadu, India. Geological Journal 55, 3615–3642. https://doi.org/10.1002/gj.3618

Taylor, D., Dalstra, H.J., Harding, A.E., Broadbent, G.C., Barley, M.E., 2001. Genesis of High-Grade Hematite Orebodies of the HamersleyProvince, Western Australia. Economic Geology 96, 837–873. https://doi.org/10.2113/gsecongeo.96.4.837

Till, J.L., Moskowitz, B.M., 2014. Deformation microstructures and magnetite texture development in synthetic shear zones. Tectonophysics 629, 211–223. https://doi.org/10.1016/j.tecto.2014.04.026

Till, J.L., Moskowitz, B.M., 2013. Magnetite deformation mechanism maps for better prediction of strain partitioning. Geophysical Research Letters 40, 697–702. https://doi.org/10.1002/grl.50170

Till, J.L., Rybacki, E., Morales, L.F.G., Naumann, M., 2019. High-Temperature Deformation Behavior of Synthetic Polycrystalline Magnetite. Journal of Geophysical Research: Solid Earth 124, 2378–2394. https://doi.org/10.1029/2018JB016903

Trimby, P.W., Prior, D.J., Wheeler, J., 1998. Grain boundary hierarchy development in a quartz mylonite. Journal of Structural Geology 20, 917–935. https://doi.org/10.1016/S0191-8141(98)00026-1

Tullis, J., 1970. Quartz: Preferred Orientation in Rocks Produced by Dauphine Twinning. Science 168, 1342–1344. https://doi.org/10.1126/science.168.3937.1342

Upadhyay, D., Mondal, S., Patel, A.K., Mishra, B., Pruseth, K.L., Bhushan, S.K., 2021. Rare earth element precipitation induced by non-redox transformation of magnetite to hematite: Microtextural and geochemical evidence from the Kamthai carbonatite complex, western India. Lithos 400–401, 106381. https://doi.org/10.1016/j.lithos.2021.106381

Valdiya, K.S., 2016. The Making of India, 2nd ed. Springer International Publishing. https://doi.org/10.1007/978-3-319-25029-8

Wheeler, J., Prior, D., Jiang, Z., Spiess, R., Trimby, P., 2001. The petrological significance of misorientations between grains. Contributions to Mineralogy and Petrology 141, 109–124. https://doi.org/10.1007/s004100000225

Yellappa, T., Chetty, T.R.K., Santosh, M., 2016. Precambrian iron formations from the Cauvery Suture Zone, Southern India: Implications for sub-marine hydrothermal origin in Neoarchean and Neoproterozoic convergent margin settings. Ore Geology Reviews 72, 1177–1196. https://doi.org/10.1016/j.oregeorev.2015.05.002

Yin, S., Wirth, R., He, H., Ma, C., Pan, J., Xing, J., Xu, J., Fu, J., Zhang, X.-N., 2022. Replacement of magnetite by hematite in hydrothermal systems: A refined redox-independent model. Earth and Planetary Science Letters 577, 117282. https://doi.org/10.1016/j.epsl.2021.117282

Zheng, Y., Han, X., Gao, X., Geng, X., Chen, X., Liu, J., 2018. Enrichment of iron ores by folding in the BIF-hosted deposit: A case study from the Archean Qian'an iron deposit, North China Craton. In: Horváth, P. (Ed.), Geological Journal 53, 617–628. https://doi.org/10.1002/gj.2916